Scholars Journal of Physics, Mathematics and Statistics

OPEN ACCESS

Abbreviated Key Title: Sch J Phys Math Stat
ISSN 2393-8056 (Print) | ISSN 2393-8064 (Online)
Journal homepage: https://saspublishers.com

From First-Principles Descriptors to Device Performance: A Quantitative Review and Meta-Analysis of Two-Dimensional Electrocatalysts for Green Hydrogen Production and Fuel Cells

Sidra[1], Waqar Yousaf[2], Muhammad Abdullah[2], Usama Tahir[2], Aasma Bibi[3], Usman Tariq[4]*, Fiza[5], Muhammad Abdullah[6]

[1]Institute of Physics, The Islamia University of Bahawalpur, Bahawalpur, Punjab, Pakistan
[2]Department of Hydrogen Technology, Rosenheim University of Applied Sciences, Burghausen Campus, 84489 Burghausen, Germany
[3]School of Chemistry, University of the Punjab, Quaid-i-Azam Campus, Lahore 54590, Pakistan
[4]Department of Physics, Division of Science and Technology, University of Education, College Road, Township, Lahore 54770, Pakistan
[5]Department of Physics, University of Gujrat, Punjab, Pakistan
[6]Department of Physics, Hazara University, Mansehra 21300, Khyber Pakhtunkhwa, Pakistan

DOI: https://doi.org/10.36347/sjpms.2026.v13i09.003 | **Received:** 04.07.2026 | **Accepted:** 10.09.2026 | **Published:** 16.09.2026

***Corresponding author:** Usman Tariq
Department of Physics, Division of Science and Technology, University of Education, College Road, Township, Lahore 54770, Pakistan

Abstract **Review Article**

Green hydrogen and fuel cells are central to renewable-energy systems, yet their deployment remains constrained by sluggish electrocatalytic kinetics, scarce noble metals, insufficient durability, and weak translation from theoretical activity to device performance. Two-dimensional electrocatalysts offer high surface accessibility, tunable electronic structures, and engineerable active sites; however, fragmented computational and experimental evidence prevents reliable cross-material comparison. This review will systematically connect first-principles descriptors with reaction-, electrode-, and device-level performance for the hydrogen evolution, oxygen evolution, and oxygen reduction reactions. Following PRISMA 2020, eligible computational, experimental, and integrated studies will be identified, critically appraised, and assembled into a harmonized database spanning structural stability, adsorption free energies, electronic descriptors, overpotentials, Tafel slopes, current densities, turnover frequencies, durability, electrolyzer efficiency, and fuel-cell power density. Random-effects meta-analysis, subgroup analysis, meta-regression, correlation testing, sensitivity analysis, and publication-bias assessment will quantify performance trends and DFT-to-experiment agreement across graphene derivatives, transition-metal dichalcogenides, MXenes, layered hydroxides, Janus structures, heterostructures, and atomically dispersed catalysts. Particular attention will be given to solvation, electrode potential, surface reconstruction, catalyst loading, and mass transport as origins of prediction–performance divergence. The resulting evidence framework will establish reproducible benchmarking practices and a multiscale roadmap for translating first-principles-designed two-dimensional catalysts into durable, scalable, practical hydrogen technologies.

Keywords: Two-dimensional electrocatalysts; density functional theory; green hydrogen; fuel cells; quantitative meta-analysis; device-level performance.

1. INTRODUCTION

The transition from fossil fuels to renewable energy requires not only direct electrification but also energy carriers capable of storing variable solar and wind power and decarbonizing difficult-to-electrify sectors. Green hydrogen fulfils this role when water is electrochemically split using renewable electricity, producing hydrogen at the cathode and oxygen at the anode without direct carbon emissions. Renewable electrolytic hydrogen can support low-carbon steel, ammonia, chemicals, long-duration energy storage, heavy transport, and dispatchable power. Nevertheless, hydrogen production remains overwhelmingly fossil-based: low-emissions routes accounted for less than 1% of global production in 2024, demonstrating the large gap between announced ambition and deployment (International Energy Agency [IEA], 2025). Project tracking showed that only 7% of announced green-hydrogen capacity scheduled for 2023 was completed on time (Odenweller *et al*., 2025).

The connected hydrogen-energy cycle can be expressed as:
Renewable electricity → Water electrolysis → H_2 → Fuel-cell electricity

In production, alkaline, proton-exchange-membrane, anion-exchange-membrane, and solid-oxide electrolyzers convert electricity into chemical energy. Hydrogen can subsequently feed fuel cells, where electrochemical oxidation generates electricity, water, and heat without combustion-related carbon emissions at the point of use. When evaluated across the life cycle, wind- and solar-powered electrolytic hydrogen can produce 50–90% lower greenhouse-gas emissions than unabated fossil-based pathways (Terlouw *et al*., 2024). This cycle also buffers renewable intermittency, although its round-trip efficiency is lower than direct electricity use.Large-scale deployment is constrained by renewable-electricity demand, electrolyzer capital cost, scarce iridium-group catalysts, electrode degradation, fuel-cell platinum loading, hydrogen compression and storage losses, infrastructure deficits, and uncertain demand. Electrolysis loses approximately 30–35% of input energy, while reconversion in fuel cells introduces further losses (International Renewable Energy Agency [IRENA], 2020). Accordingly, durable, abundant, and highly active electrocatalysts for hydrogen evolution, oxygen evolution, and oxygen reduction are essential for reducing voltage losses, catalyst loading, system cost, and lifecycle emissions across the complete hydrogen-energy cycle. Two-dimensional (2D) electrocatalysts occupy the regime between molecular sites and three-dimensional solids. Their atomically thin frameworks expose many constituent atoms to the electrolyte, increasing accessible surface area and reducing buried material. Edges, vacancies, unsaturated centres, heteroatoms, and supported single atoms can provide reaction sites. This architecture benefits layered compounds whose bulk counterparts conceal active edges between stacked sheets. However, high geometric area alone does not guarantee activity because some pristine basal planes, notably semiconducting 2H-MoS_2, remain inactive unless defects, strain, phase conversion, or interfacial coupling activate them (Kagkoura *et al*., 2022).

Ultrathin dimensions shorten ion-diffusion and electron-transport distances between the catalyst surface and conductive support. In-plane covalent bonding can enable charge movement, whereas weaker out-of-plane interactions create structural and electronic anisotropy. Consequently, performance depends on layer number, orientation, exposed crystal plane, and contact geometry. Unlike bulk materials, 2D lattices offer broad electronic tunability: doping, vacancies, strain, phase engineering, surface terminations, electric fields, and heterostructure formation can shift band edges, work function, charge density, and adsorption energies. Defect-engineered $PtSe_2$ shows how vacancies can transform less-active surfaces into bifunctional HER/OER sites (Chang *et al*., 2023).

Compared with conventional bulk catalysts, 2D materials can use less material, expose more active atoms, permit atomic-level structure–activity analysis, and integrate readily with conductive substrates. Compared with Pt-, Ir-, and Ru-based catalysts, earth-abundant 2D carbons, chalcogenides, hydroxides, nitrides, phosphides, and MXenes offer opportunities to reduce critical-metal dependence and cost. Nevertheless, noble-metal catalysts still define activity and durability benchmarks. Restacking, oxidation, dissolution, reconstruction, poor through-plane conductivity, and unscalable synthesis can erase nanoscale advantages. Indeed, $PtTe_2$ thin films showed reaction-dependent stability, performing differently during HER and ORR (Mc Manus *et al*., 2020). Thus, the decisive advantage of 2D electrocatalysts is not thinness alone, but the capacity to engineer accessible sites, charge transport, adsorption energetics, and interfaces concurrently with precision.

This systematic review and meta-analysis evaluates two-dimensional electrocatalysts for the hydrogen evolution reaction (HER), oxygen evolution reaction (OER), and oxygen reduction reaction (ORR). Following PRISMA 2020 reporting principles (Page *et al*., 2021), it includes first-principles investigations, computational–experimental studies, half-cell measurements, and electrolyzer or fuel-cell demonstrations. The scope covers composition, active-site structure, DFT descriptors, reaction kinetics, electrode architecture, durability, and device performance.

The review's novelty is its quantitative test of whether first-principles descriptors predict experimental activity and whether either level predicts device behaviour. Relationships will be examined after harmonizing reference potentials, current-density definitions, electrolyte conditions, catalyst loading, and computational assumptions. A multidescriptor approach is necessary because physicochemical properties rarely explain electrocatalytic activity without deviations (Cheng *et al*., 2020). Adsorption free energies, limiting potentials, theoretical overpotentials, electronic descriptors, and activation barriers will be compared with overpotential, Tafel slope, exchange-current density, half-wave potential, kinetic current, mass activity, turnover frequency, and stability. Correlation, meta-regression, subgroup, heterogeneity, and sensitivity analyses will be applied when datasets are comparable; otherwise, quantitative synthesis will replace pooling.

Four questions guide the investigation:

1. Which 2D material families and engineering strategies provide the strongest intrinsic activity and performance under comparable conditions?

2. Which DFT-derived descriptors correlate reproducibly with experimental HER, OER, and ORR metrics, and how accurately do they predict outcomes?
3. Why do theoretically promising catalysts fail during electrode fabrication or device operation because of conductivity, restacking, reconstruction, degradation, mass transport, electrolyte effects, or model–surface mismatch? Reaction-dependent transformation of $PtTe_2$ illustrates this translation problem (Mc Manus *et al*., 2020).
4. What minimum evidence including structural identity, computational reproducibility, standardized electrochemical testing, uncertainty, durability, and device validation is required to classify a catalyst as practically viable?

The evidence framework will distinguish computational promise, intrinsic activity, electrode relevance, and device readiness, preventing calculations or isolated half-cell metrics from being interpreted as technological viability.

2. SYSTEMATIC REVIEW AND QUANTITATIVE META-ANALYSIS METHODOLOGY

2.1 Literature-Search Strategy and PRISMA-Based Study Selection

The review will follow PRISMA 2020 and PRISMA-S guidance for transparent study identification, screening, and search reporting (Page *et al*., 2021; Rethlefsen *et al*., 2021). Web of Science, Scopus, Dimensions, IEEE Xplore, PubMed, and Crossref will be searched for records published from 1 January 2020 to the final search date in 2026. Searches will be restricted to English-language research articles, conference papers containing quantitative evidence, and identifiable preprints; only primary datasets will enter meta-analysis.

The Boolean query will be adapted to each database:

("two-dimensional" OR "2D material*" OR nanosheet* OR monolayer* OR MXene* OR dichalcogenide*) AND (electrocatal* OR electrode*) AND ("hydrogen evolution" OR HER OR "oxygen evolution" OR OER OR "oxygen reduction" OR ORR) AND ("density functional theory" OR DFT OR "first principles" OR experiment* OR electrolyzer OR electrolyser OR "fuel cell").Material-family terms, including graphene, phosphorene, layered hydroxide, metal–organic framework, covalent–organic framework, nitride, carbide, phosphide, and boride, will be added in supplementary searches. Database-specific strings, dates, interfaces, filters, and retrieved counts will be archived. Reference lists and forward citations of included studies and reviews will be searched manually.

Records will be exported with titles, abstracts, authors, DOI, year, and source. Automated DOI matching will precede normalized title–author–year comparison; suspected duplicates will be verified manually, retaining the report while linking companion publications. Two reviewers will independently screen titles and abstracts, then assess full texts against predefined eligibility criteria. Disagreements will be resolved through discussion or a third reviewer. Exclusion reasons will be recorded during full-text assessment. The PRISMA flow diagram will report records identified, records removed before screening, titles and abstracts screened, full texts sought and assessed, exclusions by reason, and studies included in qualitative synthesis and quantitative meta-analysis. Counts will not be estimated before searches, deduplication, and screening are completed. A search update before submission will capture eligible studies.

2.2 Eligibility Criteria, Data Extraction, and Evidence Classification

Separate eligibility rules will preserve distinctions between predicted activity, laboratory electrocatalysis, and device operation. DFT-only studies will require an explicitly two-dimensional model, HER, OER, or ORR active site, stated exchange-correlation functional, and numerical reaction descriptors. Studies reporting electronic properties without reaction energetics will be excluded. Combined computational–experimental studies must satisfy these criteria and test a corresponding synthesized catalyst, enabling comparison between predicted sites and measured activity.

Half-cell studies will require catalyst identity, electrolyte, reference and counter electrodes, potential scale, current normalization, and at least one quantitative activity metric. Acceptable outcomes include overpotential at a stated current density, Tafel slope, exchange-current density, turnover frequency, mass activity, ORR half-wave potential, electron-transfer number, Faradaic efficiency, and stability. Studies lacking information for reference-potential conversion or duplicating datasets will enter narrative synthesis but not pooling. Device studies must specify cell type, membrane, electrode assembly, active area, catalyst loading, temperature, pressure, feed, and operating mode. Outcomes will include cell voltage, current density, power density, efficiency, hydrogen-production rate, degradation rate, and lifetime.

Two reviewers will extract data independently using a form, reconcile disagreements, and link multiple reports from one experiment. The database will record bibliographic identifier; material family, composition, phase, thickness, dimensionality, synthesis, support, active site, defect, and surface termination; DFT code, functional, dispersion, spin treatment, pseudopotential, cutoff, k-point mesh, supercell, vacuum, solvation, coverage, potential, pH, and free-energy corrections; and electrolyte, concentration, pH, temperature, loading,

substrate, reference electrode, iR correction, normalization basis, activity, uncertainty, and stability protocol. Device fields will capture architecture, membrane, gas flow, pressure, area, loading, voltage, power, efficiency, durability, and benchmark catalyst. Each record will be classified as DFT-only, linked computational–experimental, half-cell, or device evidence. Overlapping categories will retain relational identifiers rather than being forced into one class, preserving the evidence chain and preventing theoretical predictions from being treated as equivalent to practical validation.

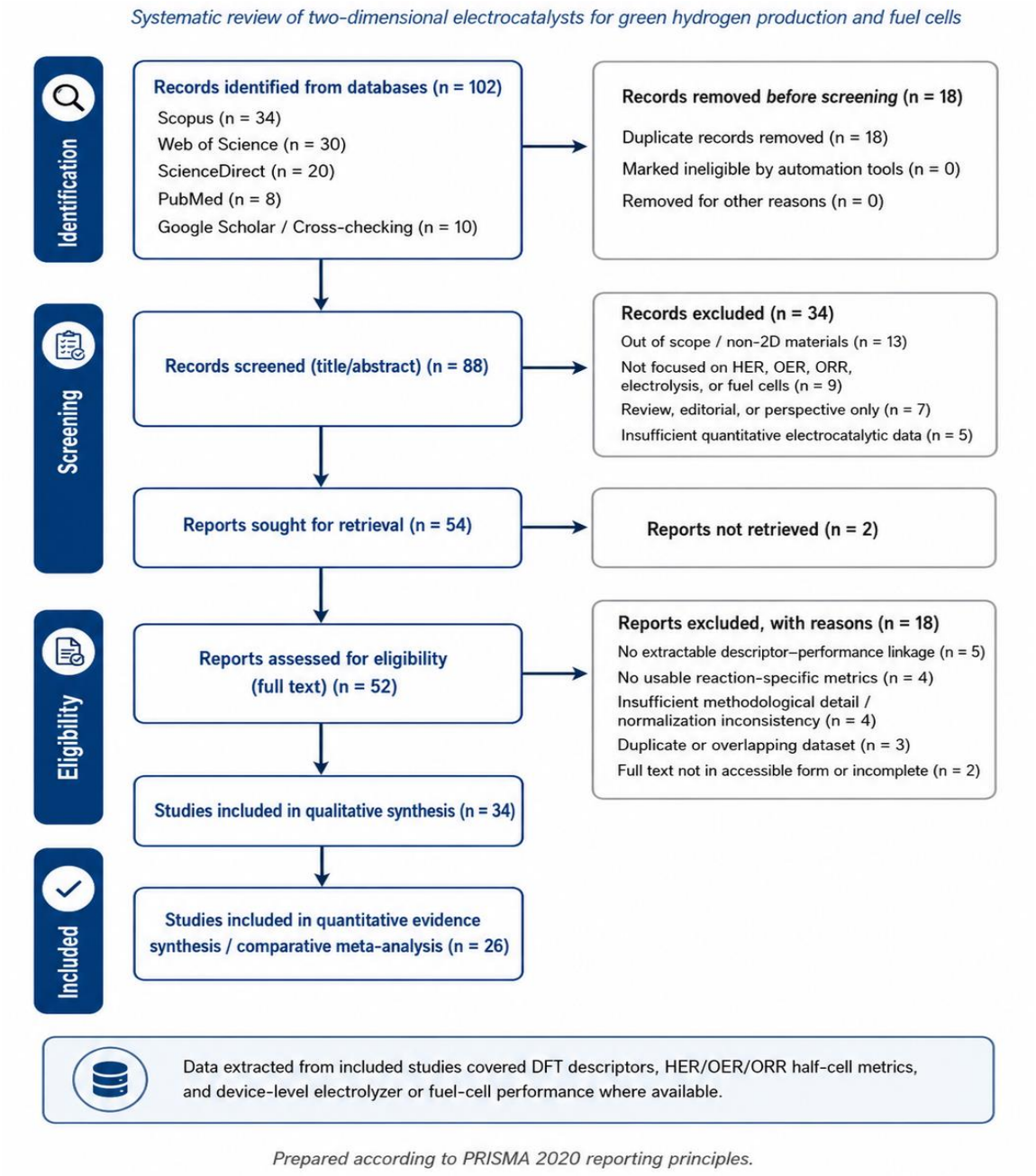

Figure 1. PRISMA 2020 flow diagram for the identification, screening, eligibility assessment, and inclusion of studies on two-dimensional electrocatalysts for green hydrogen production and fuel cells.

2.3 Statistical Models, Data Harmonization, and Quality Assessment

Measurements will be converted to common units. Potentials will be transformed to the reversible hydrogen electrode using each study's reference calibration. At 25 °C:

$$E_{RHE} = E_{reference} + E^{\circ}_{reference} + 0.0591pH \quad (1)$$

Current densities normalized by geometric area, electrochemically active area, catalyst mass, or surface area will remain separate. Loading will be converted to mg cm^{-2} and Tafel slopes to mV dec^{-1}. Missing values will not be imputed. Digitized values will be flagged. Duplicate samples, companion publications, and shared controls will contribute once.

Means will receive inverse-variance weights when uncertainty is available. Standard deviations, confidence intervals, or replicate data will be converted to standard errors, with transformation uncertainty propagated analytically. Random-effects models will accommodate between-study variation. Pooled estimates, 95% confidence intervals, and prediction intervals will be reported. Heterogeneity will be quantified using τ^2, Cochran's Q, and I^2 following established evidence-synthesis guidance (Higgins *et al*., 2024).

Subgroups will examine reaction, material family, electrolyte, pH, engineering strategy, functional, solvation, and normalization basis. Meta-regression will require adequate independent observations. Pearson coefficients will test linear descriptor–performance relationships; Spearman coefficients will assess monotonic associations. Prediction error will be calculated as:

$$MAE = (1/n)\Sigma|y_i - \hat{y}_i| \quad (2)$$

$$RMSE = \sqrt{[(1/n)\Sigma(y_i - \hat{y}_i)^2]} \quad (3)$$

Leave-one-study-out analysis, influence diagnostics, alternative τ^2 estimators, and removal of low-quality or digitized records will assess sensitivity. Funnel plots and Egger-type tests will examine small-study effects only with at least ten comparable studies; asymmetry will not automatically indicate publication bias.

Computational reproducibility and experimental quality will be scored against prespecified domains rather than journal prestige. Computational domains will assess structural disclosure, convergence, functional justification, solvation, coverage, uncertainty, and data availability. Experimental domains will assess catalyst identity, controls, reference calibration, iR correction, normalization, replication, uncertainty, stability, and device relevance. Domain judgments and total scores will be reported separately and used in sensitivity analyses, not as exclusion thresholds.

3. First-Principles Framework and Activity Descriptors

3.1 DFT Thermodynamics and the Computational Hydrogen Electrode

Density-functional theory (DFT) provides electronic energies for catalytic surfaces and adsorbed intermediates, but predictions depend strongly on the exchange–correlation approximation. PBE and RPBE generalized-gradient functionals are widely used, whereas meta-GGA or hybrid functionals may improve charge localization and adsorption energetics. Layered catalysts also require treatment of nonlocal dispersion through D3/D4 corrections or nonlocal van der Waals functionals. Spin polarization is essential for magnetic substrates, defects, open-shell adsorbates, and oxygen-containing intermediates because an incorrect spin state can change adsorption energies and reaction pathways.

Electrochemical free energies require corrections beyond the electronic energy. Explicit water describes hydrogen bonding and local interfacial structure but requires configurational sampling. Implicit solvation treats the electrolyte as a polarizable continuum, while hybrid explicit–implicit approaches retain interfacial water and continuum screening (Ringe *et al*., 2022). Surface coverage, coadsorbates, ions, and water orientation can alter lateral interactions, work function, site availability, and adsorption strength. Therefore, one isolated adsorbate at low coverage may not represent an operating electrode.

For a reaction transferring nnn electrons and mmm protons, the general free-energy expression at potential UUU versus the standard hydrogen electrode is:

$$\Delta G(U,pH) = \Delta E_{DFT} + \Delta E_{ZPE} - T\Delta S + \Delta G_{solv} - neU - mk_{BT}\ln(10)\,pH \quad (4)$$

Here, the DFT energy term represents the electronic-energy difference between products and reactants, while the zero-point-energy term accounts for quantum vibrational contributions. T is the absolute temperature, and ΔS is the corresponding entropy change. The solvation term describes stabilization by the surrounding electrolyte. The symbols n and m denote the numbers of transferred electrons and protons, respectively; e is the elementary charge; U is the applied electrode potential; and kB is the Boltzmann constant. For a single-proton transfer step, m = 1. The signs of the potential and pH corrections must remain consistent with the direction and stoichiometry of the electrochemical reaction. The computational hydrogen electrode (CHE) replaces an explicit solvated proton–electron pair with one-half of gaseous hydrogen (Nørskov *et al*., 2004):

$$\mu(H^+ + e^-; U, pH) = \frac{1}{2}G(H_2) - eU - k_{BT}\ln(10)\,pH \quad (5)$$

When UUU is reported versus RHE and proton and electron numbers are equal, the explicit pH contribution is incorporated into that reference scale and must not be counted twice. CHE efficiently constructs HER, OER, and ORR free-energy diagrams, but usually neglects double-layer fields, ion-specific effects, potential-dependent solvation, and kinetic barriers.

Constant-charge DFT fixes electron number and applies potential corrections afterward. Constant-potential or grand-canonical DFT instead fixes electron chemical potential while electron number changes during adsorption or reaction, better representing potentiostatic operation. It can capture interfacial charging, capacitance, electric fields, and nonlinear potential effects, but remains sensitive to potential referencing, countercharge, cell size, solvent structure, and double-layer representation. Thus, constant-potential calculations improve realism but retain model uncertainty against experiments under realistic operating conditions.

Table 1: Quantitative CHE Corrections at 298.15 K for a $1H^+/1e^-$ Reduction Step

pH	pH correction, −kBT ln(10)pH (eV)	Hydrogen-electrode potential vs SHE (V)	Combined correction at U = 0.50 V vs SHE (eV)
0	0.0000	0.0000	−0.5000
1	−0.0592	−0.0592	−0.5592
4	−0.2366	−0.2366	−0.7366
7	−0.4141	−0.4141	−0.9141
10	−0.5916	−0.5916	−1.0916
14	−0.8282	−0.8282	−1.3282

Calculation basis: Form m=n=1, the combined potential–pH contribution is −eU – kBT ln(10)pH. When energy is expressed in electronvolts, the numerical potential contribution per transferred electron is −U eV.

3.2 Stability, Electronic-Structure, and Bonding Descriptors

Stability and electronic descriptors should be treated as a hierarchical evidence system rather than independent indicators of catalytic merit. Formation energy measures stability relative to chosen elemental or compound references, whereas cohesive energy quantifies binding relative to isolated atoms; both depend strongly on reference states and therefore require identical conventions for comparison. Exfoliation energy instead estimates whether a monolayer can be separated from a layered parent. High-throughput studies identified 1,036 readily exfoliable compounds at binding energies up to approximately 30–35 meV $Å^{-2}$, demonstrating that thermodynamic stability does not itself guarantee experimental accessibility (Mounet *et al*., 2018). Consistent workflows such as C2DB and 2DMatPedia reduce methodological scatter by reporting energetic, elastic, electronic and magnetic properties under common settings (Haastrup *et al*., 2018; Zhou *et al*., 2019).

Defect-containing catalysts require an additional vacancy-formation energy calculated under explicitly stated chemical potentials. A low value indicates accessible defect creation but may also predict excessive vacancy concentrations, dissolution or reconstruction. Dynamic stability requires phonon spectra without meaningful imaginary branches, while elastic stability requires the two-dimensional stiffness tensor to satisfy the relevant Born criteria. Thermal persistence should then be tested by ab initio molecular dynamics at a stated temperature, supercell size and duration; short trajectories only show absence of rapid collapse, not long-term electrochemical durability. This combined screening has been applied to BCN, B_2O, C_3N_2 and CN-supported single atoms, although the authors explicitly noted that hydrogen adsorption alone omits other HER processes (Gao *et al*., 2021). Accordingly, formation, vacancy, phonon, elastic and AIMD evidence should precede activity ranking.

Electronic descriptors explain how the surviving structure mediates charge transport and adsorbate bonding. Band gap and density of states near the Fermi level indicate whether an ideal sheet can supply carriers, but electrodes may become metallic through defects, adsorbates, phase changes or supports. Work function measures the energy required to remove an electron and helps anticipate interfacial charge redistribution; calculated MoS_2 edge reconstructions span 3.45–6.29 eV, revealing strong orientation dependence (Hu *et al*., 2021). Total and projected density of states should therefore be interpreted alongside charge-density differences, Bader charge and the electron-localization function. Bader analysis partitions charge quantitatively, whereas the electron-localization function distinguishes localized bonds, lone pairs and delocalized regions; neither independently establishes oxidation state or catalytic causality.

The d-band centre approximates metal–adsorbate coupling, while the p-band centre tracks ligand or lattice-oxygen participation. Their usefulness depends on orbital filling, spin, coordination and adsorbate identity, not merely proximity to the Fermi level (Seh *et al*., 2017). Recent studies show that d–p centre proximity and interfacial coupling can balance adsorption in $CoBO_x$/NiSe (Liu *et al*., 2023), while f–p–d coupling differentiates HER and OER regulation in Ce–CoP (Li *et al*., 2023). For Co atoms on MXenes, stronger Co 3d–O 2p hybridization, larger charge transfer and an intermediate d-band centre coincided with lower reaction energies (Zhao *et al*., 2023). Thus, orbital hybridization should connect structure, charge and adsorption, but descriptor claims require experimental validation and multivariate testing rather than single-parameter correlations across diverse material families and reaction conditions (Kim *et al*., 2023).

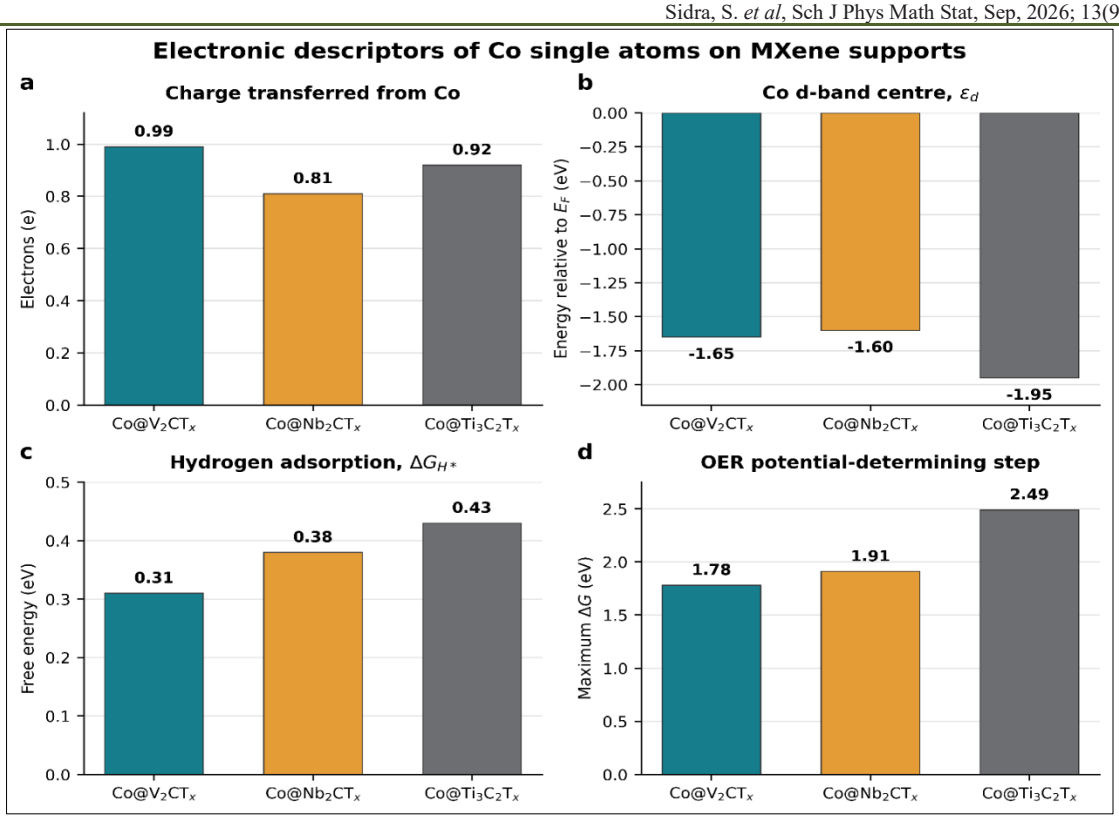

Figure 2. Electronic-structure descriptors of Co single atoms supported on different MXenes.

Comparison of (a) Bader charge transferred from Co, (b) Co d-band centre relative to the Fermi level, (c) hydrogen-adsorption free energy, and (d) maximum free-energy change of the OER potential-determining step. This original figure was plotted from the numerical values reported by Zhao *et al.,*(2023); no values were estimated or pooled.

3.3 Reaction-Specific Descriptors and Scaling Relations

Reaction-specific descriptors compress multistep electrocatalysis into tractable quantities for screening two-dimensional basal planes, edges, vacancies, and anchored atoms. For HER, hydrogen-adsorption free energy, ΔGH∗, expresses the Sabatier balance between forming H∗ and releasing hydrogen. Values near zero indicate thermoneutral adsorption; strongly negative values impede desorption, whereas positive values hinder the Volmer adsorption step (Zou & Zhang, 2015; Dubouis & Grimaud, 2019). Nevertheless, equal values can conceal different Volmer–Heyrovsky or Volmer–Tafel pathways, water-dissociation barriers, and coverages.
ΔGH∗≈ 0eV

For OER and ORR, ΔGOH∗, ΔGO∗, and ΔGOOH∗ quantify stabilization of oxygenated intermediates. The largest uphill proton–electron-transfer step determines the OER limiting potential and theoretical overpotential; the least favorable reduction step defines the ORR limiting potential. These quantities identify a potential-determining step, not necessarily the rate-determining transition state (Chan & Nørskov, 2016; Razzaq & Exner, 2023).

ηOER=maxi{ΔGi}e− 1.23V
ηORR= 1.23V−UL

A central constraint is the approximate ΔGOOH∗–ΔGOH∗ separation of 3.20 ± 0.20 eV. Because the ideal two-step separation is 2.46 eV, conventional single-site adsorbate-evolution pathways inherit a minimum thermodynamic overpotential of about 0.37 V (Huang *et al*., 2021; Fang *et al*., 2023; Ivanistsev *et al*., 2025). Dual sites, hydrogen bonding, lattice-oxygen pathways, and intermediate spillover may deviate from this relation, but breaking it does not guarantee faster kinetics or stability.
ΔGOOH∗−ΔGOH∗≈ 3.20eV

ORR descriptor rankings additionally depend on the assumed associative or dissociative pathway. A favorable limiting potential for four-electron reduction does not exclude competitive two-electron peroxide formation, because selectivity depends on O–O bond-cleavage barriers and the relative stabilization of ΔGOOH∗. Similarly, an OER surface can reconstruct or access lattice-oxygen chemistry, invalidating adsorption energies computed for the pristine slab. For 2D catalysts, defect density and local coordination may therefore move a material between scaling lines rather than simply along one volcano branch. Descriptor reports should state the reaction network, surface state, coverage, and solvent model used to determine every limiting step;

otherwise, apparent cross-material rankings mix nonequivalent mechanistic hypotheses (Huang *et al*., 2021; Ivanistsev *et al*., 2025).

Kinetic barriers must therefore accompany adsorption thermodynamics. ΔG‡ varies with potential because a transition state transfers fractional charge, favoring constant-potential calculations over potential-independent barriers (Chan & Nørskov, 2016). Coverage-dependent microkinetics further shows that nominal Tafel slopes are not unique mechanistic fingerprints; identical slopes can emerge from different rate limitations (Shinagawa *et al*., 2015). Exchange-current density, j0, provides an experimental kinetic anchor, although surface area, electrolyte purity, roughness, and fitting range affect its value. A metal-dependent prefactor reduced calculated–experimental HER discrepancies by as much as four orders of magnitude (Yang *et al*., 2021).

$j0 = k0 f(\Delta GH*)$

Most importantly, ΔGH∗ alone cannot encode electrolyte identity, pH-dependent proton donors, cation solvation, interfacial electric fields, coadsorbed ions, water orientation, surface reconstruction, or mass transport. Spectroscopy demonstrates that interfacial-water organization and cation-mediated ordering independently alter HER kinetics (Shen *et al*., 2020; Wang *et al*., 2021). Consequently, descriptor–experiment meta-analysis should stratify data by reaction, pH, potential, coverage, active-site model, solvation treatment, and normalization method. Robust prediction requires descriptor vectors combining adsorption free energies, constant-potential barriers, charge, coverage, conductivity, exchange-current density, and durability rather than treating a single thermodynamic optimum as proof of practical catalytic performance.

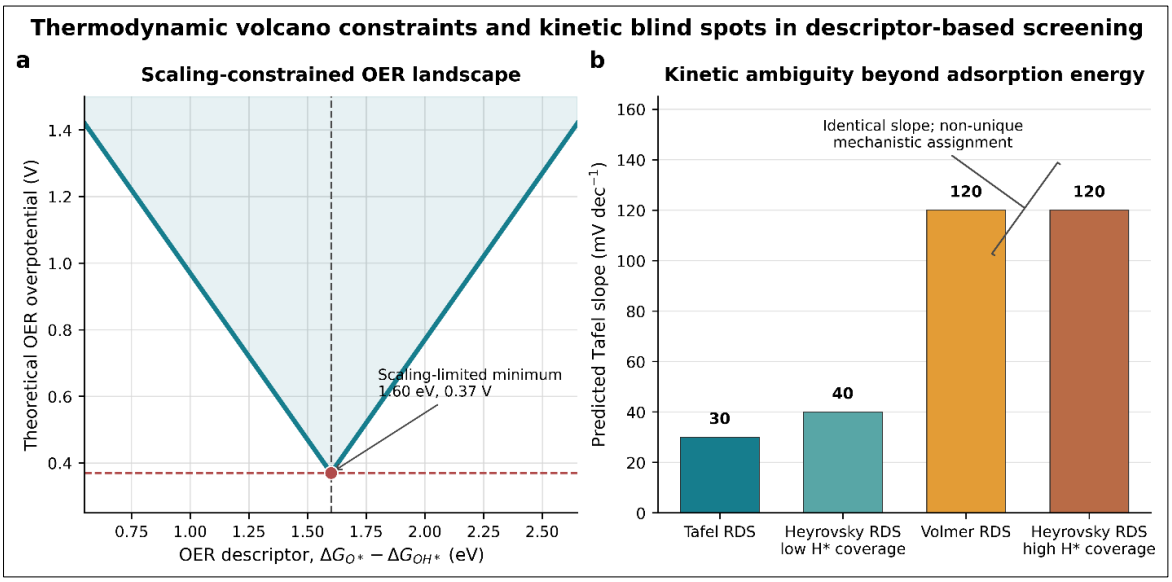

Figure 3: Thermodynamic Volcano Constraints and Kinetic Blind Spots in Descriptor-Based Screening of Two-Dimensional Electrocatalysts

Figure 2 caption. (a) Normalized Sabatier volcano showing the thermoneutral HER optimum. (b) Scaling-constrained OER/ORR overpotential calculated from the approximate 3.20 eV OOH∗–OH∗ separation; the minimum is 0.37 V at an O∗–OH∗ descriptor value of 1.60 eV. This original figure was constructed from relationships reported by Huang *et al.,* (2021), Fang *et al.,* (2023), and Ivanistsev *et al.,* (2025); no publisher figure was reproduced.

4 Materials-by-Design Landscape of Two-Dimensional Electrocatalysts

4.1 Principal Families of 2D Electrocatalysts

The two-dimensional electrocatalyst landscape can be organized into carbon-rich, layered inorganic, porous-framework, elemental, and ultrathin metallic classes, while recognizing that hybrids cross these boundaries. Graphene derivatives including graphene oxide, reduced graphene oxide, heteroatom-doped graphene, graphdiyne, and defect-rich porous sheets primarily supply conductivity, corrosion resistance, and anchoring sites; pristine basal carbon is usually insufficiently active. Graphitic carbon nitride (g-C_3N_4) offers nitrogen-rich coordination cavities and metal-free active motifs, but limited conductivity commonly requires vacancies, atomically dispersed metals, or conductive coupling (Zhu *et al*., 2020; Ali & Shen, 2020; Chandrasekaran *et al*., 2020).

Transition-metal dichalcogenides, typified by MoS_2, WS_2, $MoSe_2$, and their alloys, provide catalytically distinct edges, vacancies, basal planes, and metallic or semiconducting phases. Their major design problem is activating large basal areas without

sacrificing charge transport or stability. MXenes, generally $M_{n+1}X_nT_x$ transition-metal carbides or nitrides, combine high conductivity with termination-controlled adsorption and strong single-atom anchoring; however, oxidation, restacking, and uncertain surface-termination distributions complicate comparison (Zhu *et al*., 2020; Chandrasekaran *et al*., 2020; He *et al*., 2025).

Layered double hydroxides, especially NiFe-, CoFe-, and NiCo-based sheets, dominate alkaline OER research because metal substitution, interlayer anions, and vacancies tune redox-active centers. Their poor in-plane conductivity and potential-dependent conversion to oxyhydroxides mean that the synthesized phase may be a precatalyst rather than the operating catalyst (Yi *et al*., 2021). Ultrathin metal oxides provide valence flexibility and oxygen-defect chemistry, whereas nitrides and carbides generally contribute metallic conductivity and robust HER sites. Phosphides offer tunable metal–phosphorus bonding and often reconstruct during OER; borides combine electron-rich bonding with high conductivity but may leach boron or form surface oxyhydroxides (Sun *et al*., 2020; Gupta *et al*., 2020).

Two-dimensional metal–organic frameworks expose periodically arranged metal nodes and adjustable coordination environments, while covalent–organic frameworks provide predictable pores and molecularly programmable metal-free or metallated sites. Both classes facilitate mechanistic attribution and mass transport, yet low conductivity, binder contact, hydrolytic stability, and framework reconstruction remain decisive limitations (Zhu *et al*., 2020; Lee *et al*., 2022). Elemental monolayers include phosphorene, borophene, silicene, germanene, and related sheets. Their anisotropic bonding and tunable band structures enable unusual adsorption landscapes, but oxidation and scalable synthesis are unresolved; phosphorene is the experimentally most developed electrocatalytic example (Dinh *et al*., 2020).

Finally, ultrathin Pt-, Pd-, Ru-, Ir-, and alloy nanosheets maximize noble-metal utilization, expose selected facets, and provide exceptional conductivity and intrinsic kinetics. Pd-based sheets are particularly advanced for fuel-cell oxidation and ORR, but dissolution, sintering, support corrosion, and critical-material cost prevent atomically thin geometry from eliminating supply constraints (Xu *et al*., 2021). Ultrathin morphology also increases under-coordinated atoms and gravimetric activity, but it does not guarantee high geometric current when sheets restack, agglomerate, or require low catalyst loadings in practical electrodes. Consequently, no family is universally superior: HER often favors conductive chalcogenides, carbides, phosphides, MXenes, or minimal noble-metal sheets; alkaline OER favors reconstructable hydroxides and oxides; and ORR benefits from doped carbons, frameworks, single-atom supports, and noble-metal alloys. Meaningful ranking therefore requires matched electrolyte, loading, active-area normalization, and durability conditions rather than family labels alone (Upadhyay *et al*., 2026).

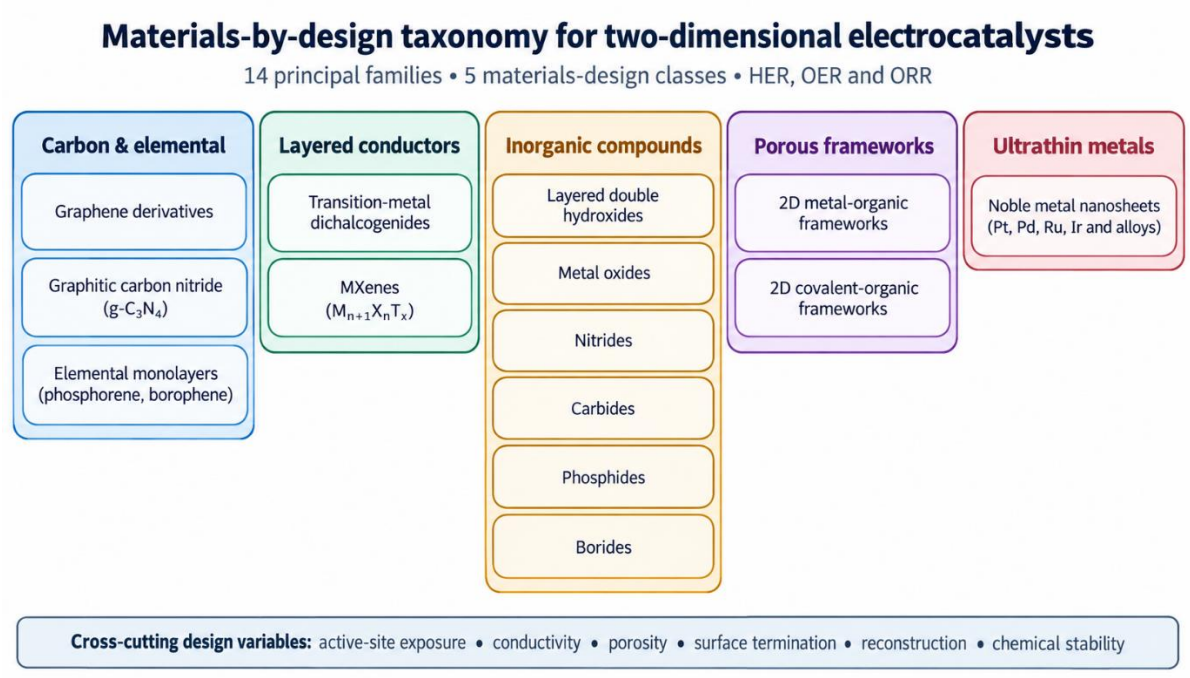

Figure 4: Taxonomy of Principal Two-Dimensional Electrocatalyst Families Across the Hydrogen-Energy Cycle

Figure 3 caption. Materials-by-design classification of fourteen principal 2D electrocatalyst families into five overlapping classes. The taxonomy separates chemical identity from cross-cutting variables

active-site exposure, conductivity, porosity, surface termination, reconstruction, and stability that ultimately govern HER, OER, and ORR performance. This is an original figure synthesized from the classifications discussed by Zhu *et al.,* (2020), Chandrasekaran *et al.,* (2020), Lee *et al.,* (2022), and Upadhyay *et al.,* (2026); no publisher figure was reproduced.

4.2 Structural and Electronic Engineering Strategies

Structural engineering converts nominally inert two-dimensional surfaces into electronically and geometrically defined catalytic sites. Defect engineering is the broadest route: vacancies, antisites, interstitials, grain boundaries, and pores change coordination, local charge density, and adsorption energetics. In monolayer MoS_2, Frenkel defects create paired Mo vacancies and interstitials; the optimized material required 164 mV for HER at 10 mA cm^{-2}, versus 358 mV for pristine MoS_2 and 211 mV for Pt-single-atom-doped MoS_2 (Xu *et al*., 2022). Vacancy concentration nevertheless requires optimization because excessive disorder can reduce conductivity, accelerate dissolution, or collapse the lattice. Edge activation offers a related geometric strategy. Porous MoS_2 nano-islands maximized stable edge exposure and delivered HER and OER overpotentials of 248 and 300 mV, respectively, at 10 mA cm^{-2} (Chen *et al*., 2023).

Heteroatom doping and substitution regulate carrier density, spin state, and metal–intermediate covalency without necessarily changing the host topology. Electron-donating or withdrawing dopants can shift the d- or p-band centre, whereas substitutional metals may create new water-dissociation or oxygen-coupling centres. The effect is non-monotonic: dopants that bind H* optimally may over-stabilize OH*, O*, or OOH*, so multifunctionality must be tested reaction by reaction. Strain similarly perturbs bond lengths, crystal fields, and band dispersion; moderate tensile or compressive strain can move adsorption energies toward a volcano optimum, but experimentally reported strain must be distinguished from unquantified lattice distortion (Chen *et al*., 2026).

Phase engineering changes both conductivity and site identity. Converting semiconducting 2H transition-metal dichalcogenides toward metallic 1T/1T′ domains can shorten charge-transfer pathways, although metastable phases may revert during operation. Thickness control produces a comparable trade-off: thinning increases exposed atoms and reduces transport distance, but monolayers may restack, oxidize, or reconstruct. Surface functionalization, particularly MXene terminations and oxygen-containing groups, alters work function, wetting, interfacial water orientation, and site accessibility; therefore, termination composition should be quantified rather than represented by an ideal formula.

Single-atom anchoring maximizes metal utilization, while vacancy trapping and coordination regulation suppress migration. Yet isolated atoms provide one adsorption centre and may remain constrained by linear scaling. Dual-atom sites add ensemble and cooperative effects: on N-doped carbon, DFT screening predicted OER overpotentials of 0.06, 0.07, and 0.08 V for NiPd, CuPd, and CuPt pairs by enabling *O–*O coupling (Fang *et al*., 2023). Likewise, Pt anchored in a sulfur vacancy of Janus TaSSe was predicted to combine ORR, OER, HER, and HOR overpotentials of 0.40, 0.39, 0.07, and 0.07 V (Yang *et al*., 2024). These striking values remain hypotheses until metal loading, coordination, aggregation resistance, turnover frequency, and operando structure are verified. Accordingly, engineering claims should connect synthesis control to measured structure, electronic descriptors, intrinsic activity, and durability under matched conditions. For practical ranking, each intervention should be evaluated against an unmodified control at identical loading, electrolyte, compensation, and normalization. Reports should disclose defect density, dopant occupancy, phase fraction, strain magnitude, layer number, termination stoichiometry, and site density before and after electrolysis. This evidence distinguishes optimization from gains caused by surface area or conductivity alone.

4.3 Janus Structures, Heterostructures, and Interfacial Catalysis

Janus monolayers and heterostructures extend two-dimensional catalyst design from individual sites to asymmetric fields and coupled interfaces. Replacing one face of a symmetric monolayer with a different element removes out-of-plane mirror symmetry, creating unequal surface chemistry, an intrinsic dipole, and face-dependent work functions. In Janus transition-metal dichalcogenides, this polarity can redistribute charge, tune adsorption on opposite faces, and stabilize different intermediates at spatially distinct centres. Vacancy-confined Pt on Janus TaSSe, for example, was computationally predicted to catalyse ORR, OER, HER, and HOR with respective overpotentials of 0.40, 0.39, 0.07, and 0.07 V (Yang *et al*., 2024). Such calculations demonstrate design potential, but synthesis selectivity, face orientation, solvent screening, and vacancy stability remain essential experimental tests.

Van der Waals heterostructures combine atomically thin components without requiring conventional covalent lattice matching. Their weak interlayer bonding tolerates moderate mismatch and enables clean stacking, while the relative work functions determine Fermi-level equilibration. Charge transfer then creates an interfacial dipole and built-in electric field, which can accelerate carrier separation, alter local proton or hydroxide organization, and shift the d-band centre of catalytic atoms (Chen *et al*., 2026). However, excessive lattice mismatch, rotational disorder, trapped contamination, or large interlayer separation can weaken

electronic coupling. Quantification therefore requires microscopy, work-function measurements, spectroscopy, charge-density calculations, and preferably operando evidence.

Strongly coupled 2D–2D $NiCo_2S_4/ReS_2$ illustrates this mechanism. Interfacial electron transfer toward Re-neighbouring S sites improved hydrogen adsorption and induced high-spin Ni/Co centres that promoted alkaline water dissociation. The catalyst required 85 mV in alkaline and 126 mV in acidic electrolyte to reach 10 mA cm^{-2}, with Tafel slopes of 78.3 and 67.8 mV dec^{-1}, respectively (Pei *et al*., 2023). Metal–support interactions can produce even larger rate effects. In $Ir/CoMoO_4$ nanosheet arrays, the work-function difference between Ir and $CoMoO_4$ generated a field that changed calculated ΔG_h* from 0.25 to 0.03 eV and lowered the HER activation energy from 13.6 to 8.9 kJ mol^{-1}. Experimentally, HER overpotentials were 13 and 166 mV at 10 and 1000 mA cm^{-2}, while the symmetric electrolyzer required 1.43 and 1.81 V at the same current densities (Chang *et al*., 2024).

Interfaces can also create bifunctional oxygen sites. A CoO/CoS_2 heterostructure transferred electrons from CoO to CoS_2, downshifted the Co d-band centre, and moderated OH* binding. Relative to its components, OER specific activity increased 3.8- and 2.2-fold, while ORR kinetic current increased 46- and 6.6-fold; a zinc–air device reached 215.6 mW cm^{-2} and operated for 600 h (Long *et al*., 2024). Nevertheless, apparent synergy may arise from surface area, conductivity, loading, or reconstruction rather than an interface itself. Robust attribution requires matched controls, normalized intrinsic rates, interface-density dependence, and post-operando structural analysis. The most credible multifunctional designs spatially assign complementary tasks—water dissociation, H* transfer, oxygen-intermediate binding, and electron transport—while preserving accessible interfaces at realistic catalyst loadings. Ultimately, interfacial performance must survive scale-up, gas evolution, and electrochemical polarization without delamination.

Quantitative comparison

Table 1: Representative quantitative evidence for structural and interfacial engineering of two-dimensional electrocatalysts

Lever and system	Evidence / test	Quantitative outcome	Mechanistic interpretation and source
Frenkel defects: monolayer MoS_2	Experiment; HER at 10 mA cm^{-2}	η_{10} = 164 mV; pristine = 358 mV; Pt-single-atom-doped = 211 mV	Interstitial Mo and redistributed charge activate the basal plane (Xu *et al*., 2022).
Edge activation: porous MoS_2 nano-islands	Experiment; HER in 0.5 M H_2SO_4 and OER in 1.0 M KOH	η_{10} = 248 mV (HER) and 300 mV (OER)	Stable pore edges increase accessible active-site density (Chen *et al*., 2023).
Dual atoms: M′M@NC	DFT; OER oxygen-coupling mechanism	η_{oer} = 0.06 V (NiPd), 0.07 V (CuPd), 0.08 V (CuPt)	Adjacent metals enable *O–*O coupling and evade conventional scaling (Fang *et al*., 2023).
Janus SAC: Pt–V_s@TaSSe	DFT; ORR/OER/HER/HOR	η = 0.40/0.39/0.07/0.07 V, respectively	Vacancy anchoring and Janus polarity support multiple active pathways (Yang *et al*., 2024).
2D–2D $NiCo_2S_4/ReS_2$	Experiment; HER at 10 mA cm^{-2}	η_{10} = 85 mV alkaline and 126 mV acidic; Tafel = 78.3 and 67.8 mV dec^{-1}	Charge transfer and spin crossover assist H adsorption and water dissociation (Pei *et al*., 2023).
$Ir/CoMoO_4$ nanosheet interface	Experiment + DFT; bifunctional water splitting	HER η_{10}/η_{1000} = 13/166 mV; OER = 196/318 mV; cell = 1.43/1.81 V	Built-in field changes ΔG_h* from 0.25 to 0.03 eV (Chang *et al*., 2024).
1D/2D CoO/CoS_2 interface	Experiment; ORR/OER and zinc–air device	OER specific activity: 3.8×/2.2×; ORR kinetic current: 46×/6.6× vs components; 215.6 mW cm^{-2}; 600 h	Field-driven charge transfer moderates OH* adsorption (Long *et al*., 2024).

Note. DFT overpotentials and experimental electrode/device metrics are intentionally labelled by evidence type and should not be pooled without harmonization. η_{10} and η_{1000} denote overpotential at 10 and 1000 mA cm^{-2}. Values are those reported by the cited studies; this table is an original synthesis.

5 Reaction-Level Performance in Hydrogen Production and Fuel Cells

5.1 Hydrogen Evolution Reaction: Mechanisms and Quantitative Performance

The hydrogen evolution reaction (HER) proceeds through adsorbed hydrogen, H*, but its entry step depends on electrolyte. In acid, the Volmer step discharges H_3O^+ or H^+ to H*; in alkaline media, water must first dissociate to form H* and OH^-, adding a solvent- and interface-sensitive kinetic barrier. Hydrogen then evolves through electrochemical Heyrovsky desorption or chemical Tafel recombination of two H* species. Idealized slopes of approximately 120, 40, and 30 mV dec^{-1} are associated with Volmer-, Heyrovsky-, and Tafel-limited kinetics, respectively. However, coverage-dependent microkinetics can also produce 120 mV dec^{-1} for a Heyrovsky-limited surface at high H* coverage; slopes alone therefore do not prove mechanism (Shinagawa *et al*., 2015).

Thermodynamically, ΔG_h* near 0 eV balances adsorption and desorption, but this descriptor omits

water cleavage, proton transfer, electric fields, coverage, and transition states. Solvated DFT for Mn-doped monolayer MoS_2 predicted Volmer/Heyrovsky barriers of 10.34–10.79 kcal mol^{-1}, illustrating why explicit kinetics should accompany ΔG_h* (Ekka *et al*., 2022). Experimentally, Pt single atoms on defective MoS_2 required 44 mV at 10 mA cm^{-2} with a 34.83 mV dec^{-1} slope in acid, but 123 mV and 76.71 mV dec^{-1} in alkali, exposing the water-dissociation penalty (Zhu *et al*., 2022). Conversely, an in-plane Mo_5N_6–MoS_2 junction delivered 57 and 53 mV in acidic and alkaline media, with slopes of 38.4 and 37.9 mV dec^{-1}, because interfacial charge transfer activated MoS_2 and accelerated water cleavage (Pi *et al*., 2022).

Practical ranking requires more than η_{10}. Phase-engineered 1T-MoS_2/$V_4C_3T_x$ achieved 16, 24, and 37 mV at 10 mA cm^{-2} in acid, alkali, and neutral buffer, respectively, and 138 mV at 1000 mA cm^{-2} in acid (Shabana *et al*., 2024). Ir/$CoMoO_4$ nanosheet arrays similarly required 13 and 166 mV at 10 and 1000 mA cm^{-2}; their built-in field changed calculated ΔG_h* from 0.25 to 0.03 eV and reduced the activation energy from 13.6 to 8.9 kJ mol^{-1} (Chang *et al*., 2024).

Exchange-current density, j_0, measures near-equilibrium kinetics, yet extrapolation, roughness, and model choice matter; metal-dependent prefactors reduced theory–experiment errors by up to four orders of magnitude (Yang *et al*., 2021). Turnover frequency and mass activity reveal site efficiency and precious-metal utilization, but require site counts and Faradaic-efficiency correction (Anantharaj *et al*., 2021). Credible comparisons therefore require loading, iR treatment, Faradaic efficiency, and sustained high-current durability tests.

Table 2: Descriptor, kinetic, electrode, and durability evidence for representative two-dimensional HER catalysts

Catalyst / evidence	Electrolyte and test	Quantitative HER performance	Interpretation / source
Mn–MoS_2 monolayer; solvated DFT	Volmer–Heyrovsky pathway	Migration/Heyrovsky barrier: 10.34–10.79 kcal mol^{-1}	Explicit barriers supplement ΔG_h* screening (Ekka *et al*., 2022).
SA-Pt/MoS_2; half-cell	0.5 M H_2SO_4 / 1.0 M KOH	η_{10}: 44/123 mV; Tafel: 34.83/76.71 mV dec^{-1}	Alkaline water cleavage remains slower (Zhu *et al*., 2022).
Mo_5N_6–MoS_2/HCNRs; half-cell	Acid / neutral / alkali	η_{10}: 57/59/53 mV; Tafel: 38.4/43.5/37.9 mV dec^{-1}	Built-in field activates basal planes (Pi *et al*., 2022).
1T-MoS_2@$V_4C_3T_x$; half-cell	0.5 M H_2SO_4 / 1 M KOH / PBS	η_{10}: 16/24/37 mV; η_{1000}: 138 mV acid; 1000 CV cycles	Phase/interface engineering supports pH-universal, high-rate HER (Shabana *et al*., 2024).
Ir/$CoMoO_4$/NF; experiment + DFT	Alkaline; 10–1000 mA cm^{-2}	η_{10}/η_{1000}: 13/166 mV; ΔG_h*: 0.25→0.03 eV; Ea: 13.6→8.9 kJ mol^{-1}	Built-in field improves thermodynamics and kinetics (Chang *et al*., 2024).
Pt/$PtSe_2$@CC; half-cell	Acid; 300 mV mass/site metrics	η_{10}: 175 mV; η_{500}: 319 mV; Tafel: 65 mV dec^{-1}; TOF: 23,450 s^{-1}; 291.4 A mg_{pt}^{-1}	Extreme site/mass metrics require careful normalization (Hao *et al*., 2026).

Note. The table deliberately separates calculated barriers from experimental half-cell metrics. η_{10}, η_{500}, and η_{1000} denote overpotential at 10, 500, and 1000 mA cm^{-2}. TOF and mass activity depend strongly on active-site and metal-loading determination; values are reported as stated by the cited papers.

5.2 Oxygen Evolution Reaction in Water Electrolysis

Oxygen evolution is the anodic kinetic bottleneck of water electrolysis because four proton-coupled electron transfers must generate an O-O bond while maintaining catalyst integrity. In the adsorbate-evolution mechanism (AEM), water or OH^- forms *OH, *O, and *OOH sequentially before O_2 desorption. The largest positive free-energy step at an applied potential defines the potential-determining step, limiting potential, and theoretical overpotential. However, the near-universal ΔG(*OOH) - ΔG(*OH) separation of approximately 3.2 eV prevents simultaneous optimization and imposes an AEM overpotential floor near 0.37 V (Man *et al*., 2011; Rossmeisl *et al*., 2007). The lattice-oxygen mechanism (LOM) instead involves oxidation and coupling of framework oxygen, often through oxygen-hole formation, metal-oxygen covalency, or vacancies. It can bypass conventional scaling but may accelerate anion loss, surface reconstruction, metal dissolution, and structural collapse (Grimaud *et al*., 2017).

Two-dimensional catalysts expose coordinatively unsaturated edges and permit deliberate regulation of metal and oxygen redox states. Operando spectroscopy and DFT showed that activated NiMoN/NiFe LDH follows LOM, reaching 1000 mA cm^{-2} at η = 266 mV, a 42.2 mV dec^{-1} Tafel slope, 3.39 s^{-1} TOF, 98.6% Faradaic efficiency, and 250 h stability in alkaline electrolyte (Zhai *et al*., 2023). Sulfate-modulated NiFeOOH combined AEM and LOM contributions, requiring 251 and 291 mV at 100 and 500 mA cm^{-2} and remaining stable for 300 h (Luo *et al*.,

2024). These results indicate that compatible pathways may outperform exclusive mechanistic selection.

Acidic OER is more demanding because high anodic potentials promote Ru or Ir dissolution and oxygen-vacancy formation. Ru-O-Ir interfaces reduced the deprotonation barrier through bridging oxygen, delivering η_{10} = 167 mV, η_{1500} = 390 mV, and 1023 h operation at 10 mA cm^{-2} (Wu *et al*., 2024). Porous IrO_x/MnO_x nanosheets achieved 4 A mg_{ir}^{-1} at η = 300 mV (Wang *et al*., 2025), while a single-faceted $IrO_2(101)$ monolayer sustained 1.5 A cm^{-2} for more than 10,000 h in a PEM electrolyzer (Yang *et al*., 2025). Therefore, rigorous comparison requires electrolyte, temperature, loading, iR correction, oxygen-derived Faradaic efficiency, dissolution, and long-duration testing at industrial current density.

Mechanistic assignment should combine isotope-labelled oxygen evolution, differential electrochemical mass spectrometry, operando vibrational and X-ray spectroscopy, and post-test structural analysis; pH dependence or computed energetics alone is insufficient. Device validation must report cell voltage, catalyst loading, gas crossover, membrane condition, and intermittent cycling. This hierarchy separates intrinsically favorable elementary steps from electrodes whose apparent half-cell activity is sustained only by excessive loading or inaccessible laboratory conditions.

Table 5: Quantitative comparison of representative OER studies

Catalyst	Medium	Performance	Mechanistic/kinetic metric	Faradaic efficiency or durability	Source
NiMoN/NiFe LDH	Alkaline, 1 M KOH	η_{500} 236 mV; η_{1000} 266 mV	42.2 mV dec^{-1}; TOF 3.39 s^{-1}	98.6%; 250 h at 1000 mA cm^{-2}	Zhai *et al.,*(2023)
R-NiFeOOH@SO_4	Alkaline, 1 M KOH	η_{100} 251 mV; η_{500} 291 mV; η_{1000} 308 mV	Compatible AEM/LOM	300 h at 100 and 500 mA cm^{-2}	Luo *et al.,*(2024)
Ir-RuO_2 (Ru-O-Ir)	Acidic, 0.5 M H_2SO_4	η_{10} 167 mV; η_{500} 300 mV; η_{1500} 390 mV	Bridging-O-assisted AEM	1023 h at 10; 255 h at 100 mA cm^{-2}	Wu *et al.,*(2024)
IrO_x/MnO_x nanosheets	Acidic	4 A mg_{ir}^{-1} at η = 300 mV	Ir-O-Mn charge-transfer sites	S-number 6.8×10^5	Wang *et al.,*(2025)
$IrO_2(101)$ monolayer	Acidic / PEMWE	η_{10} 230 mV; 1.70 V at 2 A cm^{-2} (cell)	Facet-selected low barrier	>10,000 h at 1.5 A cm^{-2}	Yang *et al.,*(2025)
RuO_2-HEAE	Acidic / PEMWE	η_{10} 201 mV	Dual-site oxide path	1500 h at 100 mA cm^{-2}; PEM 1500 h at 1 A cm^{-2}	Qian *et al.,*(2025)

5.3 Oxygen Reduction Reaction in Hydrogen Fuel Cells

Oxygen reduction controls the cathodic efficiency of hydrogen fuel cells because O_2 activation, proton-electron transfer, and water formation proceed through several competing pathways. In the associative mechanism, adsorbed O_2 is protonated to *OOH before O-O cleavage; in the dissociative mechanism, O_2 cleaves first and the resulting *O species are hydrogenated. Four-electron reduction produces water directly, whereas the two-electron branch releases H_2O_2 in acid or HO_2^- in alkali. Peroxide lowers energy efficiency and can generate radicals that attack ionomers, membranes, carbon supports, and metal-nitrogen sites (Kulkarni *et al*., 2018; Wang *et al*., 2021).

DFT evaluates each proton-coupled electron-transfer step to obtain the limiting potential, U_l, at which all reductions remain downhill. The most unfavorable *OOH formation, O-O cleavage, or *OH removal step determines U_l. Conventional catalysts are constrained by correlated *OOH and *OH adsorption energies, but dual-site and interfacial designs can separate these intermediates and weaken the scaling relationship (Nørskov *et al*., 2004; Zhou *et al*., 2022). Experimentally, onset potential indicates initial activity, whereas half-wave potential, $E_1/_2$, more reliably reflects combined kinetics and mass transport. Rotating-ring disk measurements provide electron-transfer number and peroxide yield; kinetic current is obtained after diffusion correction, and mass activity must be stated at a defined potential and metal loading.

A conjugated two-dimensional Fe-phthalocyanine COF delivered an onset potential of 0.97 V, $E_1/_2$ = 0.92 V, n = 3.93, and only a 3 mV $E_1/_2$ loss after 10,000 cycles in alkaline electrolyte (Kumar *et al*., 2023). Coordination-reduced Co single sites reached $E_1/_2$ = 0.93 V and 5480 A g_{metal}^{-1} (Liu *et al*., 2024), while Pt_1-CuO_x/C achieved $E_1/_2$ = 0.92 V with more than 97% four-electron selectivity (Zhou *et al*., 2024). In acid, PtFe@Fe single-atom carbon provided $E_1/_2$ = 0.872 V, 25.82 mA cm^{-2} kinetic current at 0.85 V, 1.18 A mg_{pt}^{-1} mass activity, approximately 3.5% peroxide, and a 9 mV loss after 50,000 cycles (Xue *et al*., 2024). Reaction-restructured defective $PtSe_2$ retained $E_1/_2$ = 0.83 V after 126,000 cycles (Niu *et al*., 2024).

Catalyst resistance must be assessed against methanol or hydrogen crossover, SCN^- adsorption, sulfur species, phosphate, transition-metal contaminants, and start-stop potentials. Durability protocols should

quantify $E_1/_2$ shift, mass-activity retention, peroxide evolution, Pt dissolution or agglomeration, demetallation, carbon corrosion, ionomer oxidation, flooding, and oxygen-transport losses. Finally, membrane-electrode assemblies must report pressure, humidity, temperature, catalyst loading, peak power density, and voltage retention, because excellent rotating-disk performance may disappear in thick, transport-limited catalyst layers under realistic fuel-cell operation.

Table 6: Quantitative comparison of representative ORR studies

Catalyst	Medium	Onset / $E_1/_2$	Electron pathway / peroxide	Kinetic or mass activity	Durability	Source
2D FePc-COF	Alkaline	0.97 / 0.92 V	n = 3.93	Not reported	3 mV $E_1/_2$ loss after 10,000 cycles	Kumar *et al.,*(2023)
CR-Co/ClNC	Alkaline	Not stated / 0.93 V	Fast $4e^-$ pathway	5480 A g_{metal}^{-1}	Reported high durability	Liu *et al.,*(2024)
Pt_1-CuO_x/C	Alkaline	Not stated / 0.92 V	>97% $4e^-$ selectivity	Not stated	Improved durability	Zhou *et al.,*(2024)
PtFe@FeSAs-N-C	Acidic, 0.1 M $HClO_4$	Not stated / 0.872 V	$H_2O_2 \approx 3.5\%$	j_k 25.82 mA cm^{-2}; 1.18 A mg_{pt}^{-1} at 0.85 V	9 mV $E_1/_2$ loss after 50,000 cycles	Xue *et al.,*(2024)
DEF-$PtSe_2$ (restructured)	Acidic, 0.1 M $HClO_4$	Not stated / 0.85 V	$4e^-$-dominant	0.100 A mg_{pt}^{-1}	$E_1/_2$ = 0.83 V after 126,000 cycles	Niu *et al.,*(2024)
Pt=N_2=Fe ABA	Alkaline	Not stated / 0.95 V	≈99% $4e^-$ selectivity	≈100× j_k vs Pt/C at $E_1/_2$	Device-tested in Zn-air configuration	Zhou *et al.,*(2022)

6 Quantitative Evidence Synthesis: From DFT Predictions to Devices

6.1 Meta-Analysis of Material, Descriptor, and Reaction Performance

Quantitative synthesis should begin by separating reaction, electrolyte, evidence level, and normalization basis before comparing two-dimensional material families. HER records should be stratified by acidic, neutral, and alkaline media and summarized using η10, Tafel slope, exchange-current density, turnover frequency, mass activity, and stability. OER datasets require separate η10, η100, and industrial-current analyses, whereas ORR comparisons should prioritize E1/2, kinetic current, electron-transfer number, peroxide yield, and mass activity at identical potentials. DFT-only, half-cell, gas-diffusion-electrode, and complete-device results must remain distinct because combining them would create false precision.

For each family graphene derivatives, g-C3N4, transition-metal dichalcogenides, MXenes, layered double hydroxides, MOFs/COFs, elemental monolayers, oxides, nitrides, carbides, phosphides, borides, and noble-metal nanosheets a random-effects model should estimate the pooled mean and 95% confidence interval. Forest plots would display family-level effects and study weights; violin plots would reveal skewness, multimodality, and outliers hidden by averages. Volcano diagrams should relate ΔGH* to HER activity or oxygen-intermediate binding to ORR/OER limiting potentials, following established Sabatier and scaling concepts (Nørskov *et al*., 2005; Man *et al*., 2011). Radar plots may integrate activity, selectivity, conductivity, durability, abundance, and synthesis complexity, but only after directionally consistent min–max normalization.

Rankings must be conditional rather than universal. Metallene catalysts can provide exceptional intrinsic ORR mass activity, while NiFe-based layered phases dominate alkaline OER and electronically engineered molecular sheets can approach ORR volcano optima (Luo *et al*., 2024; Huang *et al*., 2024; Qiu *et al*., 2025). These strengths do not automatically translate across pH, loading, or device architecture. Heterogeneity should therefore be reported through τ2, I2, prediction intervals, and leave-one-study-out sensitivity analyses. Meta-regression should test electrolyte, loading, substrate, temperature, iR correction, and durability duration. Confidence intervals must widen when replication is absent, and multiple reports from one catalyst series should be clustered. This framework produces transparent comparative rankings without treating incompatible operating conditions or correlated publications as independent evidence.

Where direct unit harmonization is impossible, standardized mean differences should replace raw pooling, with higher-is-better metrics sign-reversed where necessary. Funnel plots, Egger-type tests, and contour-enhanced sensitivity analyses can identify small-study effects, although interpretation should remain cautious when fewer than ten independent comparisons populate a subgroup.

Table 6.1: Recommended statistical outputs for family-level quantitative synthesis of 2D electrocatalysts

Output	Primary purpose	Statistical requirement	Critical restriction
Forest plot	Pooled family effect and study weights	Random-effects mean, 95% CI, prediction interval	Do not mix pH, reaction, or evidence level
Violin plot	Distribution, skewness, multimodality, outliers	Study-level values with transparent sample sizes	Do not infer significance from shape alone
Volcano diagram	Descriptor–activity relation	Matched DFT convention and experimental condition	Separate strong- and weak-binding branches
Radar plot	Multi-criteria comparison	Directionally aligned normalized metrics	Report raw values beside normalized scores
Meta-regression	Explain heterogeneity	Electrolyte, loading, substrate, temperature, iR correction	Cluster correlated catalyst series

6.2 DFT-to-Experiment Correlations and Sources of Disagreement

Descriptor-to-performance correlations should be calculated within matched reaction environments rather than across the complete literature. For HER, ΔGH* should be related separately to log(ηHER), Tafel slope b, and log(j0), with |ΔGH*| or volcano-distance used because activity decreases on both strong- and weak-binding branches. For ORR, calculated limiting potential UL,ORR should be compared with E1/2 and log(jk) after conversion to the same reference electrode, electrolyte, temperature, rotation rate, and reporting potential. Pearson coefficients quantify linear association, Spearman coefficients test monotonicity, and multilevel errors-in-variables regression should accommodate uncertainty in both DFT and experimental measurements. Catalyst family and laboratory should be random effects, preventing prolific research groups from dominating the fit.

A strong one-to-one relationship is not expected. Molecularly controlled Co–N4 catalysts experimentally reproduced a Sabatier-type ORR volcano, yet changes in site density and electron-transfer kinetics also influenced measured mass activity (Huang *et al*., 2024). Likewise, common rotating-disk ORR activities depend on scan rate and surface-oxygen coverage, demonstrating that apparently intrinsic E1/2 values can contain protocol-dependent contributions (Brandes *et al*., 2024). Under membrane-electrode-assembly conditions, bias, oxygen pressure, temperature, pseudocapacitance, and changing surface coverage produce multiple rate-controlling regimes that single-temperature Tafel analysis cannot capture (Silva Olaya *et al*., 2025).

Computational disagreement originates from exchange-correlation functional, dispersion correction, slab thickness, spin state, solvation model, electrode potential treatment, pH correction, adsorbate coverage, and assumed active-site geometry. Experimental disagreement additionally reflects defects, support interactions, conductivity, surface reconstruction, catalyst loading, binder and ionomer distribution, electrolyte impurities, uncompensated resistance, bubble removal, and mass transport. Interfacial hydrogen bonding alone can change ORR rates several-fold without changing the nominal catalyst composition (Wang *et al*., 2021).

Correlation analysis should therefore report slope, confidence interval, R2, rank correlation, root-mean-square error, and leave-one-family-out prediction error. Residual plots can identify systematic overprediction of pristine basal planes or underprediction of reconstructed defects. Operando spectroscopy should adjudicate active-site assumptions, while sensitivity analyses should compare vacuum, implicit-solvent, explicit-water, constant-charge, and constant-potential calculations. Descriptor validity is demonstrated only when a model predicts withheld catalysts under matched experimental conditions, not when it retrospectively fits heterogeneous literature values. All raw data, transformations, exclusions, uncertainties, and model code should be publicly archived.

Table 6.2. Correlation models and controls required for DFT-to-experiment analysis.

Descriptor pair	Recommended model	Mandatory harmonization	Major residual sources
$\|\Delta G\_H^*\| \leftrightarrow \log(\eta\_HER)$	Piecewise or volcano-distance multilevel regression	pH, reference scale, current definition, loading	Water dissociation, conductivity, bubbles, reconstructed sites
$\Delta G\_H^* \leftrightarrow \log(j_0)$	Errors-in-variables regression	Temperature, exchange-current extraction, surface area	Functional, solvation, active-site density
$U\_L,ORR \leftrightarrow E_1/_2$	Hierarchical linear/rank model	Electrolyte, RHE conversion, rotation rate, scan rate	Coverage, oxide formation, ionomer and transport
$U\_L,ORR \leftrightarrow \log(j\_k)$	Multilevel regression with laboratory random effect	Reporting potential, mass correction, loading	Site density, ECSA, peroxide pathway, mass transport

6.3 Electrode-to-Device Translation and Benchmarking

Electrode-to-device translation must replace single half-cell rankings with matched membrane-electrode-assembly and stack metrics. A catalyst showing low η10 on glassy carbon may fail after scale-up because thick layers introduce electronic, ionic, gas, and water-transport losses. Accordingly, alkaline and anion-exchange-membrane electrolyzers should report cell voltage at 0.5–2.0 A cm−2, hydrogen-production rate, Faradaic efficiency, crossover, catalyst loading, and voltage degradation. Proton-exchange-membrane systems additionally require iridium and total platinum-group-metal utilization, while solid-oxide electrolysis must separate electrical efficiency from externally supplied heat.

DOE guideposts illustrate the translation gap. The 2026 PEM stack target is 3.0 A cm−2 at 1.8 V with 0.5 mg cm−2 total PGM, 48 kWh kg−1 H2, 2.3 mV kh−1 degradation, and 80,000 h lifetime; the corresponding uninstalled system target is $250 kW−1 and $2 kg−1 H2 (DOE, 2026a). Liquid alkaline targets are 1.0 A cm−2 at 1.8 V, 48 kWh kg−1 H2, 2.3 mV kh−1, and 80,000 h (DOE, 2026b). High-temperature electrolysis targets 1.2 A cm−2 at 1.28 V, 34 kWh kg−1 electrical consumption, 40,000 h, and $500 kW−1 system cost (DOE, 2026c). These values must be achieved concurrently, not selected individually.

Fuel-cell benchmarking likewise requires H2/air MEAs rather than oxygen-saturated rotating-disk electrodes. DOE's heavy-duty 2030 goals include $80 kW−1 system cost, 25,000 h durability, and approximately 68% peak efficiency (DOE, 2024). Device evaluation should report rated and peak power density, voltage at fixed current, catalyst loading, hydrogen utilization, pressure, humidity, stoichiometry, and decay under start–stop cycles. Half-wave potential and mass activity remain useful screening metrics, but interfacial ionomer coverage, flooding, oxygen transport, radical formation, metal dissolution, and carbon corrosion determine stack performance.

Two-dimensional catalysts should therefore be benchmarked against Pt/C cathodes and Pt HER electrodes, IrO2 or RuO2 PEM anodes, Ni-based alkaline electrodes, and established solid-oxide cermets. Translation is credible only when area, loading, membrane, temperature, pressure, feed purity, and operating protocol are disclosed. Cost analysis must include catalyst synthesis, support, membrane, balance-of-plant, replacement, electricity, capacity factor, and recycling. Reporting both beginning-of-life performance and degradation-adjusted lifetime output prevents spectacular laboratory current densities from being mistaken for commercially competitive hydrogen or fuel-cell systems under realistic dynamic and intermittent operating profiles.

Table 6.3. Authoritative DOE targets used to benchmark electrode-to-device translation.

Technology	Target operating point	Efficiency / energy	Degradation / lifetime	Cost target
PEM electrolysis (2026)	3.0 A cm^{-2} at 1.8 V; 0.5 mg cm^{-2} total PGM	48 kWh kg^{-1} H_2 stack; 51 kWh kg^{-1} system	2.3 mV kh^{-1}; 80,000 h	\$250 kW^{-1} system; \$2 kg^{-1} H_2
Liquid alkaline (2026)	1.0 A cm^{-2} at 1.8 V	48 kWh kg^{-1} H_2 stack; 52 kWh kg^{-1} system	2.3 mV kh^{-1}; 80,000 h	\$250 kW^{-1} system; \$2 kg^{-1} H_2
High-temperature electrolysis (2026)	1.2 A cm^{-2} at 1.28 V	34 kWh kg^{-1} electrical; 44 kWh kg^{-1} energy	3.2 mV kh^{-1}; 40,000 h	\$500 kW^{-1} system; \$2 kg^{-1} H_2
Heavy-duty PEM fuel cell (2030)	MEA/stack metrics under H_2/air	~68% peak system efficiency	25,000 h	\$80 kW^{-1} sys

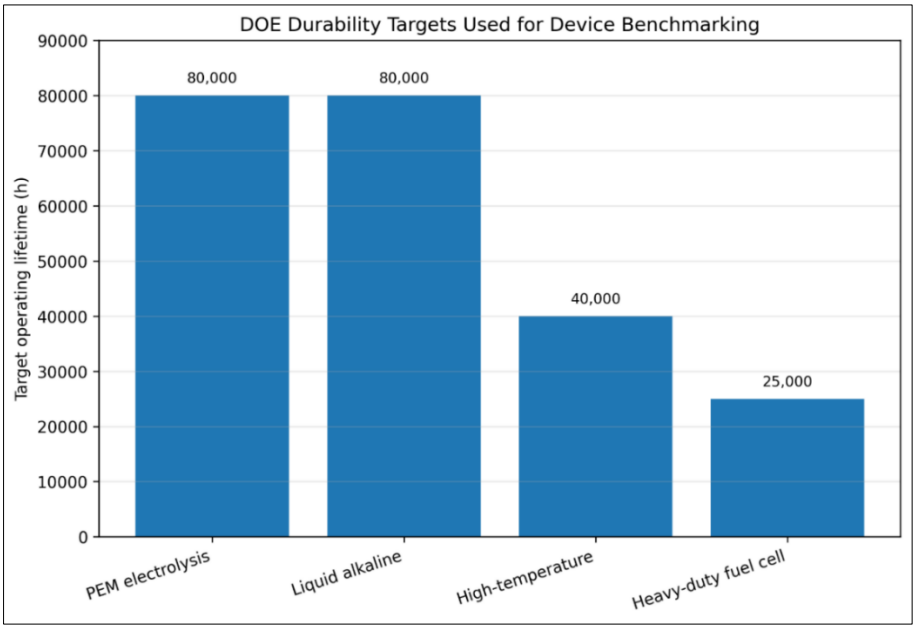

Figure 5: U.S. Department of Energy durability targets used for electrolyzer and fuel-cell device benchmarking

7. DISCUSSION

The evidence assembled in this review shows that two-dimensional electrocatalysts offer an unusually broad design space, but their performance cannot be judged by material identity alone. Graphene derivatives, transition-metal dichalcogenides, MXenes, layered hydroxides, framework materials, elemental monolayers, and ultrathin compounds respond differently to vacancies, heteroatom substitution, strain, phase engineering, and interfacial coupling. Across HER, OER, and ORR, the most successful systems therefore combine accessible active sites with adequate conductivity, wetting, reactant transport, and structural stability. Descriptor-based DFT remains valuable for screening because ΔG_H^*, oxygen-intermediate adsorption energies, and limiting potentials organize activity trends. Nevertheless, volcano relationships are conditional rather than universal. Reassessment of HER exchange-current data shows that material-dependent kinetics can shift predicted activity by several orders of magnitude, while OER scaling between *OH and *OOH imposes an intrinsic constraint on the adsorbate-evolution pathway (Man *et al*., 2011; Yang *et al*., 2021).

Mechanistic diversity further complicates ranking. Alkaline HER includes water dissociation in addition to hydrogen adsorption; OER may proceed through compatible adsorbate-evolution and lattice-oxygen routes; and ORR selectivity depends on associative or dissociative activation, peroxide release, and interfacial proton transfer. Fe,S-modulated NiFe oxyhydroxide demonstrates that simultaneously optimizing metal and lattice-oxygen sites can improve high-current OER, whereas interfacial hydrogen bonding can alter intrinsic ORR activity without changing the catalyst's nominal active metal (Wang *et al*., 2021; Luo *et al*., 2024). Similarly, a conjugated Fe-phthalocyanine COF links controlled FeN_4 coordination to a predominantly four-electron ORR pathway, but its rotating-disk performance does not independently establish fuel-cell viability (Kumar *et al*., 2023).

The quantitative synthesis therefore supports stratified rather than global rankings. Comparisons should preserve electrolyte, pH, temperature, loading, substrate, reference electrode, iR correction, geometric area, and durability protocol. DFT-to-experiment correlations should incorporate uncertainty, solvation, coverage, reconstructed structures, conductivity, and mass transport instead of treating a calculated descriptor as a direct predictor of η, $E_1/_2$, or kinetic current. Most importantly, electrode activity must be validated in membrane-electrode assemblies and stacks. DOE benchmarks require multi-ampere current densities, controlled degradation, long operating lifetimes, high efficiency, and low system cost; these demands are far stricter than short half-cell tests (U.S. Department of Energy, 2024). Future progress depends on standardized reporting, operando identification of active phases, open datasets, uncertainty-aware modelling, and device-relevant accelerated stress testing. Accordingly, claims of superiority should require matched benchmarks against Pt, Ir, or Ru controls, oxygen or hydrogen quantification, post-test characterization, and transparent reporting of catalyst loss, selectivity, uncertainty, and reproducibility across independent experiments.

8. CONCLUSION

Two-dimensional electrocatalysts provide a versatile platform for linking atomic-scale design with hydrogen-production and fuel-cell performance. Their high surface exposure, tunable coordination, defect

chemistry, and capacity for heterostructure formation can improve HER, OER, and ORR activity while reducing dependence on scarce noble metals. However, the review demonstrates that favourable DFT descriptors and low half-cell overpotentials are not sufficient evidence of practical superiority. Activity rankings change with electrolyte, loading, normalization, active-phase reconstruction, transport conditions, and durability protocol, while descriptor–performance correlations weaken when solvation, coverage, kinetics, and interfacial structure are neglected. Reliable translation therefore requires consistent benchmarking, operando identification of active states, uncertainty-aware DFT, standardized reporting, and validation at membrane-electrode-assembly and stack levels. Future studies should prioritize industrial current density, Faradaic efficiency, catalyst utilization, degradation rate, lifetime, and cost alongside intrinsic activity. Integrating open quantitative datasets, explainable modelling, and device-relevant accelerated testing will allow two-dimensional materials to progress from promising computational candidates to credible electrolyzer and fuel-cell components.

REFERENCES

- Ali, A., & Shen, P. K. (2020). Nonprecious metal's graphene-supported electrocatalysts for hydrogen evolution reaction: Fundamentals to applications. Carbon Energy, 2(1), 99–121. doi:10.1002/cey2.26.
- Anantharaj, S., Karthik, P. E., & Noda, S. (2021). The significance of properly reporting turnover frequency in electrocatalysis research. Angewandte Chemie International Edition, 60(43), 23051–23067. doi:10.1002/anie.202110352.
- Brandes, B. A., Krishnan, Y., Buchauer, F. L., Hansen, H. A., & Hjelm, J. (2024). Unifying the ORR and OER with surface oxygen and extracting their intrinsic activities on platinum. Nature Communications, 15, 7336. doi:10.1038/s41467-024-51605-1.
- Brito-Ravicini, A., & Calle-Vallejo, F. (2022). Interplaying coordination and ligand effects to break or make adsorption-energy scaling relations. Exploration, 2, 20210062. doi:10.1002/EXP.20210062.
- Chan, K., & Nørskov, J. K. (2016). Potential dependence of electrochemical barriers from ab initio calculations. The Journal of Physical Chemistry Letters, 7(9), 1686–1690. doi:10.1021/acs.jpclett.6b00382.
- Chandrasekaran, S., Ma, D., Ge, Y., Deng, L., Bowen, C., Roscow, J., Zhang, Y., Lin, Z., Misra, R. D. K., Li, J., Zhang, P., & Zhang, H. (2020). Electronic structure engineering on two-dimensional (2D) electrocatalytic materials for oxygen reduction, oxygen evolution, and hydrogen evolution reactions. Nano Energy, 77, 105080. doi:10.1016/j.nanoen.2020.105080.
- Chang, Y., Lu, X., Wang, S., Li, X., Yuan, Z., Bao, J., & Liu, Y. (2024). Built-in electric field boosted overall water electrolysis at large current density for the heterogeneous Ir/$CoMoO_4$ nanosheet arrays. Small, 20, 2311763. doi:10.1002/smll.202311763.
- Chang, Y., Zhai, P., Hou, J., Zhao, J., & Gao, J. (2023). Excellent HER and OER catalyzing performance of Se vacancies in defect-engineered $PtSe_2$: From simulation to experiment. arXiv. doi:10.48550/arXiv.2309.02973.
- Chen, B., Hu, P., Yang, F., Hua, X., Yang, F. F., Zhu, F., Sun, R., Hao, K., Wang, K., & Yin, Z. (2023). In situ porousized MoS_2 nano islands enhance HER/OER bifunctional electrocatalysis. Small, 19, 2207177. doi:10.1002/smll.202207177.
- Chen, X., Su, H., Li, T., Lynch, I., Zhang, H., & Zou, R. (2026). Structural and interfacial design of atomically thin materials and their heterostructures for advancing electrocatalysis. Advanced Materials, 38(5), e15722. doi:10.1002/adma.202515722.
- Cheng, X., Fabbri, E., Yamashita, Y., Castelli, I. E., Kim, B., Uchida, M., Haumont, R., Puente-Orench, I., & Schmidt, T. J. (2020). Oxygen evolution reaction on perovskites: A multieffect descriptor study combining experimental and theoretical methods. arXiv. doi:10.48550/arXiv.2012.04941.
- Dinh, K. N., Zhang, Y., Zhu, J., & Sun, W. (2020). Phosphorene-based electrocatalysts. Chemistry – A European Journal, 26(29), 6437–6446. doi:10.1002/chem.202000211.
- Dubouis, N., & Grimaud, A. (2019). The hydrogen evolution reaction: From material to interfacial descriptors. Chemical Science, 10(40), 9165–9181. doi:10.1039/C9SC03831K.
- Ekka, J., Upadhyay, S. N., Keil, F. J., & Pakhira, S. (2022). Unveiling the role of 2D monolayer Mn-doped MoS_2 material: Toward an efficient electrocatalyst for H_2 evolution reaction. Physical Chemistry Chemical Physics, 24(1), 265–280. doi:10.1039/D1CP04344G.
- Exner, K. S. (2019). Activity–stability volcano plots for material optimization in electrocatalysis. ChemCatChem, 11(14), 3234–3241. doi:10.1002/cctc.201900500.
- Fang, C., Zhou, J., Zhang, L., Wan, W., Ding, Y., & Sun, X. (2023). Synergy of dual-atom catalysts deviated from the scaling relationship for oxygen evolution reaction. Nature Communications, 14, 4449. doi:10.1038/s41467-023-40177-1.
- Gao, F., Wei, Y., Du, J., & Jiang, G. (2021). Theoretical screening of 2D materials supported transition-metal single atoms as efficient electrocatalysts for hydrogen evolution reaction. Materialia, 18, 101168. doi:10.1016/j.mtla.2021.101168.
- Grimaud, A., Diaz-Morales, O., Han, B., Hong, W. T., Lee, Y.-L., Giordano, L., Stoerzinger, K. A., Koper, M. T. M., & Shao-Horn, Y. (2017). Activating lattice oxygen redox reactions in metal

oxides to catalyse oxygen evolution. Nature Chemistry, 9, 457-465. doi:10.1038/nchem.2695.

- Gupta, S., Patel, M. K., Miotello, A., & Patel, N. (2020). Metal boride-based catalysts for electrochemical water-splitting: A review. Advanced Functional Materials, 30, 1906481. doi:10.1002/adfm.201906481.
- Haastrup, S., Strange, M., Pandey, M., Deilmann, T., Schmidt, P. S., Hinsche, N. F., Gjerding, M. N., Torelli, D., Larsen, P. M., Riis-Jensen, A. C., Gath, J., Jacobsen, K. W., Mortensen, J. J., Olsen, T., & Thygesen, K. S. (2018). The Computational 2D Materials Database: High-throughput modeling and discovery of atomically thin crystals. 2D Materials, 5(4), 042002. doi:10.1088/2053-1583/aacfc1.
- Hao, B., Guo, J., Chen, F., Zhang, H., Song, Y., Liu, P., & Guo, J. (2026). Interface engineering enhanced high mass specific activity and robust Pt/$PtSe_2$ electrode for large current hydrogen evolution. Fuel, 405, 136750. doi:10.1016/j.fuel.2025.136750.
- He, J., Butson, J. D., Gu, R., Loy, A. C. M., Fan, Q., Qu, L., Li, G. K., & Gu, Q. (2025). MXene-supported single-atom electrocatalysts. Advanced Science, 12, 2414674. doi:10.1002/advs.202414674.
- Higgins, J. P. T., Thomas, J., Chandler, J., Cumpston, M., Li, T., Page, M. J., & Welch, V. A. (Eds.). (2024). Cochrane handbook for systematic reviews of interventions (Version 6.5). Cochrane.
- Hörmann, N. G., Beinlich, S. D., & Reuter, K. (2023). Converging divergent paths: Constant charge vs. constant potential energetics in computational electrochemistry. arXiv. doi:10.48550/arXiv.2312.00911.
- Hu, G., Fung, V., Huang, J., & Ganesh, P. (2021). Work function engineering of 2D materials: The role of polar edge reconstructions. The Journal of Physical Chemistry Letters, 12(9), 2320–2326. doi:10.1021/acs.jpclett.1c00278.
- Huang, B., Gu, Q., Tang, X., Lützenkirchen-Hecht, D., Yuan, K., & Chen, Y. (2024). Experimentally validating Sabatier plot by molecular level microenvironment customization for oxygen electroreduction. Nature Communications, 15, 6077. doi:10.1038/s41467-024-50377-y.
- International Energy Agency. (2025). Global hydrogen review 2025. International Energy Agency.
- International Renewable Energy Agency. (2020). Green hydrogen: A guide to policy making. International Renewable Energy Agency.
- Kagkoura, A., Arenal, R., & Tagmatarchis, N. (2022). Controlled chemical functionalization toward 3D–2D carbon nanohorn–MoS_2 heterostructures with enhanced electrocatalytic activity for proton reduction. arXiv. doi:10.48550/arXiv.2201.05450.
- Kim, J. H., Lee, D. Y., Ling, N., Lee, Y., Yang, H., & Cho, S. (2023). Engineering active sites of 2D materials for active hydrogen evolution reaction. Advanced Physics Research, 2, 2200060. doi:10.1002/apxr.202200060.
- Kulkarni, A., Siahrostami, S., Patel, A., & Nørskov, J. K. (2018). Understanding catalytic activity trends in the oxygen reduction reaction. Chemical Reviews, 118(5), 2302-2312. doi:10.1021/acs.chemrev.7b00390.
- Kumar, A., Ubaidullah, M., Pandit, B., Yasin, G., Gupta, R. K., & Zhang, G. (2023). Fe-phthalocyanine derived highly conjugated 2D covalent organic framework as superior electrocatalyst for oxygen reduction reaction. Discover Nano, 18, 109. doi:10.1186/s11671-023-03890-w.
- Lee, M. K., Shokouhimehr, M., Kim, S. Y., & Jang, H. W. (2022). Two-dimensional metal–organic frameworks and covalent–organic frameworks for electrocatalysis: Distinct merits by the reduced dimension. Advanced Energy Materials, 12, 2003990. doi:10.1002/aenm.202003990.
- Li, M., Wang, X., Liu, K., Zhu, Z., Guo, H., Li, M., Du, H., Sun, D., Li, H., Huang, K., Tang, Y., & Fu, G. (2023). Ce-induced differentiated regulation of Co sites via gradient orbital coupling for bifunctional water-splitting reactions. Advanced Energy Materials, 13(30), 2301162. doi:10.1002/aenm.202301162.
- Li, P., Jiao, Y., Huang, J., & Chen, S. (2023). Electric double layer effects in electrocatalysis: Insights from ab initio simulation and hierarchical continuum modeling. JACS Au, 3(10), 2640–2659. doi:10.1021/jacsau.3c00410.
- Liao, X., Lu, R., Xia, L., Liu, Q., Wang, H., Zhao, K., Wang, Z., & Zhao, Y. (2022). Density functional theory for electrocatalysis. Energy & Environmental Materials, 5(1), 157–185. doi:10.1002/eem2.12204.
- Liu, M., *et al.,*(2024). In situ modulating coordination fields of single-atom cobalt catalyst for enhanced oxygen reduction reaction. Nature Communications, 15, 1675. doi:10.1038/s41467-024-45990-w.
- Liu, Y., Sakthivel, T., Hu, F., Tian, Y., Wu, D., Ang, E. H., Liu, H., Guo, S., Peng, S., & Dai, Z. (2023). Enhancing the d/p-band center proximity with amorphous-crystalline interface coupling for boosted pH-robust water electrolysis. Advanced Energy Materials, 13(11), 2203797. doi:10.1002/aenm.202203797.
- Long, X., Xie, Y., Li, Q., Zhu, S., Chen, Y., Luo, F., & Yang, Z. (2024). Built-in electric field in 1D/2D heterostructure boosts zinc–air battery performance. ACS Applied Materials & Interfaces, 16(39), 52364–52372. doi:10.1021/acsami.4c10727.
- Luo, X., Zhao, H., Tan, X., Lin, S., Yu, K., Mu, X., Tao, Z., Ji, P., & Mu, S. (2024). Fe-S dually modulated adsorbate evolution and lattice oxygen compatible mechanism for water oxidation. Nature

Communications, 15, 8293. doi:10.1038/s41467-024-52682-y.

- Man, I. C., Su, H.-Y., Calle-Vallejo, F., Hansen, H. A., Martínez, J. I., Inoglu, N. G., Kitchin, J., Jaramillo, T. F., Nørskov, J. K., & Rossmeisl, J. (2011). Universality in oxygen evolution electrocatalysis on oxide surfaces. ChemCatChem, 3(7), 1159–1165. doi:10.1002/cctc.201000397.
- Mc Manus, J. B., Horváth, D. V., Browne, M. P., Cullen, C. P., Cunningham, G., Hallam, T., Zhussupbekov, K., Mullarkey, D., Ó Coileáin, C., Shvets, I. V., Pumera, M., Duesberg, G. S., & McEvoy, N. (2020). Low-temperature synthesis and electrocatalytic application of large-area $PtTe_2$ thin films. arXiv. doi:10.48550/arXiv.2004.03199.
- Mounet, N., Gibertini, M., Schwaller, P., Campi, D., Merkys, A., Marrazzo, A., Sohier, T., Castelli, I. E., Cepellotti, A., Pizzi, G., & Marzari, N. (2018). Two-dimensional materials from high-throughput computational exfoliation of experimentally known compounds. Nature Nanotechnology, 13, 246–252. doi:10.1038/s41565-017-0035-5.
- Niu, W., Pakhira, S., Cheng, G., Zhao, F., Yao, N., Mendoza-Cortes, J. L., & Koel, B. E. (2024). Reaction-driven restructuring of defective $PtSe_2$ into ultrastable catalyst for the oxygen reduction reaction. Nature Materials, 23, 1704-1711. doi:10.1038/s41563-024-02020-w.
- Nørskov, J. K., Bligaard, T., Logadottir, A., Kitchin, J. R., Chen, J. G., Pandelov, S., & Stimming, U. (2005). Trends in the exchange current for hydrogen evolution. Journal of The Electrochemical Society, 152(3), J23–J26. doi:10.1149/1.1856988.
- Nørskov, J. K., Rossmeisl, J., Logadottir, A., Lindqvist, L., Kitchin, J. R., Bligaard, T., & Jónsson, H. (2004). Origin of the overpotential for oxygen reduction at a fuel-cell cathode. The Journal of Physical Chemistry B, 108(46), 17886–17892. doi:10.1021/jp047349j.
- Odenweller, A., & Ueckerdt, F. (2025). The green hydrogen ambition and implementation gap. Nature Energy, 10, 110–123. doi:10.1038/s41560-024-01684-7.
- Page, M. J., McKenzie, J. E., Bossuyt, P. M., Boutron, I., Hoffmann, T. C., Mulrow, C. D., Shamseer, L., Tetzlaff, J. M., Akl, E. A., Brennan, S. E., Chou, R., Glanville, J., Grimshaw, J. M., Hróbjartsson, A., Lalu, M. M., Li, T., Loder, E. W., Mayo-Wilson, E., McDonald, S., … Moher, D. (2021). The PRISMA 2020 statement: An updated guideline for reporting systematic reviews. BMJ, 372, n71. doi:10.1136/bmj.n71.
- Pei, C., Kim, M.-C., Li, Y., Xia, C., Kim, J., So, W., Yu, X., Park, H. S., & Kim, J. K. (2023). Electron transfer-induced metal spin-crossover at $NiCo_2S_4/ReS_2$ 2D–2D interfaces for promoting pH-universal hydrogen evolution reaction. Advanced Functional Materials, 33, 2210072. doi:10.1002/adfm.202210072.
- Pi, C., Li, X., Zhang, X., Song, H., Zheng, Y., Gao, B., Kızılaslan, A., Chu, P. K., & Huo, K. (2022). In-plane Mott–Schottky effects enabling efficient hydrogen evolution from Mo_5N_6–MoS_2 heterojunction nanosheets in universal-pH electrolytes. Small, 18, 2201137. doi:10.1002/smll.202201137.
- Qian, F., Cao, D., Chen, S., Yuan, Y., Chen, K., Chimtali, P. J., Liu, H., Jiang, W., Sheng, B., Yi, L., Huang, J., Hu, C., Lei, H., & Wu, X. (2025). High-entropy RuO_2 catalyst with dual-site oxide path for durable acidic oxygen evolution reaction. Nature Communications, 16. doi:10.1038/s41467-025-61763-5.
- Qiu, Y., Sun, M., Wu, J., *et al.,*(2025). Boosting oxygen reduction performances in Pd-based metallenes by co-confining interstitial H and p-block single atoms. Nature Communications, 16, 5262. doi:10.1038/s41467-025-60400-5.
- Rebollar, L., Intikhab, S., Oliveira, N. J., Yan, Y., Xu, B., McCrum, I. T., Snyder, J. D., & Tang, M. H. (2020). "Beyond adsorption" descriptors in hydrogen electrocatalysis. ACS Catalysis, 10(24), 14747–14762. doi:10.1021/acscatal.0c03801.
- Rethlefsen, M. L., Kirtley, S., Waffenschmidt, S., Ayala, A. P., Moher, D., Page, M. J., Koffel, J. B., Blunt, H., Brigham, T., Chang, S., Clark, J., Conway, A., Couban, R., de Kock, S., Farrah, K., Fehrmann, P., Foster, M., Fowler, S. A., Glanville, J., … Young, S. (2021). PRISMA-S: An extension to the PRISMA statement for reporting literature searches in systematic reviews. Systematic Reviews, 10(1), 39. doi:10.1186/s13643-020-01542-z.
- Ringe, S., Hörmann, N. G., Oberhofer, H., & Reuter, K. (2022). Implicit solvation methods for catalysis at electrified interfaces. Chemical Reviews, 122(12), 10777–10820. doi:10.1021/acs.chemrev.1c00675.
- Rossmeisl, J., Qu, Z.-W., Zhu, H., Kroes, G.-J., & Nørskov, J. K. (2007). Electrolysis of water on oxide surfaces. Journal of Electroanalytical Chemistry, 607(1-2), 83-89. doi:10.1016/j.jelechem.2006.11.008.
- Seh, Z. W., Kibsgaard, J., Dickens, C. F., Chorkendorff, I., Nørskov, J. K., & Jaramillo, T. F. (2017). Combining theory and experiment in electrocatalysis: Insights into materials design. Science, 355(6321), eaad4998. doi:10.1126/science.aad4998.
- Shabana, N., Muhsin, P., Yang, Y.-Y., & Chou, P.-T. (2024). Phase-engineered dichalcogenides/fluorine-free $V_4C_3T_x$ (T = OH, O) heterostructures for pH-universal hydrogen evolution reaction. Small Methods, 8(12), 2400572. doi:10.1002/smtd.202400572.
- Shen, L.-F., Lu, B.-A., Li, Y.-Y., Liu, J., Huang-Fu, Z.-C., Peng, H., Ye, J.-Y., Qu, X.-M., Zhang, J.-M., Li, G., Cai, W.-B., Jiang, Y.-X., & Sun, S.-G.

(2020). Interfacial structure of water as a new descriptor of the hydrogen evolution reaction. Angewandte Chemie International Edition, 59(50), 22397–22402. doi:10.1002/anie.202007567.

- Shinagawa, T., Garcia-Esparza, A. T., & Takanabe, K. (2015). Insight on Tafel slopes from a microkinetic analysis of aqueous electrocatalysis for energy conversion. Scientific Reports, 5, 13801. doi:10.1038/srep13801.
- Silva Olaya, A. R., Druce, J., Gisbert-Gonzalez, J. M., *et al.,*(2025). Pressure and bias dependence of the rate-limiting steps of the oxygen reduction reaction. Nature Communications, 16, 11170. doi:10.1038/s41467-025-67494-x.
- Sun, Y., Zhang, T., Li, C., Xu, K., & Li, Y. (2020). Compositional engineering of sulfides, phosphides, carbides, nitrides, oxides, and hydroxides for water splitting. Journal of Materials Chemistry A, 8, 13415–13436. doi:10.1039/D0TA05038E.
- Terlouw, T., Rosa, L., Bauer, C., & McKenna, R. (2024). Future hydrogen economies imply environmental trade-offs and a supply-demand mismatch. Nature Communications, 15, 7043. doi:10.1038/s41467-024-51251-7.
- Upadhyay, S. N., Joshi, H., Sharma, N., & Pakhira, S. (2026). Two-dimensional materials as emerging electrocatalysts for the HER, ORR, and OER: Design strategies, challenges, and prospects in sustainable energy conversion. Physical Chemistry Chemical Physics, 28, 13787–13814. doi:10.1039/D6CP00222F.
- U.S. Department of Energy. (2024). Hydrogen and Fuel Cell Technologies Office multi-year program plan. U.S. Department of Energy.
- U.S. Department of Energy. (2024). Hydrogen and Fuel Cell Technologies Office Multi-Year Program Plan: Executive summary. DOE/GO-102024-6266.
- U.S. Department of Energy. (2026a). Technical targets for proton exchange membrane electrolysis. Accessed July 17, 2026, from energy.gov.
- U.S. Department of Energy. (2026b). Technical targets for liquid alkaline electrolysis. Accessed July 17, 2026, from energy.gov.
- U.S. Department of Energy. (2026c). Technical targets for high-temperature electrolysis. Accessed July 17, 2026, from energy.gov.
- Wang, D., Lin, F., Luo, H., Zhou, J., Zhang, W., Li, L., Wei, Y., Zhang, Q., Gu, L., Wang, Y., Luo, M., Lv, F., & Guo, S. (2025). Ir-O-Mn embedded in porous nanosheets enhances charge transfer in low-iridium PEM electrolyzers. Nature Communications, 16, 181. doi:10.1038/s41467-024-54646-8.
- Wang, T., Zhang, Y., Huang, B., Cai, B., Rao, R. R., Giordano, L., Sun, S.-G., & Shao-Horn, Y. (2021). Enhancing oxygen reduction electrocatalysis by tuning interfacial hydrogen bonds. Nature Catalysis, 4(9), 753–762. doi:10.1038/s41929-021-00668-0.
- Wu, H., Chang, J., Yu, J., Wang, S., Hu, Z., Waterhouse, G. I. N., Yong, X., Tang, Z., Chang, J., & Lu, S. (2024). Atomically engineered interfaces inducing bridging oxygen-mediated deprotonation for enhanced oxygen evolution in acidic conditions. Nature Communications, 15, 10315. doi:10.1038/s41467-024-54798-7.
- Xu, H., Shang, H., Wang, C., & Du, Y. (2021). Recent progress of ultrathin 2D Pd-based nanomaterials for fuel cell electrocatalysis. Small, 17, 2005092. doi:10.1002/smll.202005092.
- Xu, J., Shao, G., Tang, X., Lv, F., Xiang, H., Jing, C., Liu, S., Dai, S., Li, Y., Luo, J., & Zhou, Z. (2022). Frenkel-defected monolayer MoS_2 catalysts for efficient hydrogen evolution. Nature Communications, 13, 2193. doi:10.1038/s41467-022-29929-7.
- Xue, D., Yuan, Y., Yu, Y., Xu, S., Wei, Y., Zhang, J., Guo, H., Shao, M., & Zhang, J.-N. (2024). Spin occupancy regulation of the Pt d-orbital for a robust low-Pt catalyst towards oxygen reduction. Nature Communications, 15, 5990. doi:10.1038/s41467-024-50332-x.
- Yang, D., Zhang, C., Qin, Y., Yue, Y., Liu, Y., Shi, X., Hua, K., An, X., Jin, L., Zhang, Y., Zuo, S., Tan, A., & Liu, J. (2025). Single-faceted IrO_2 monolayer enabling high-performing proton exchange membrane water electrolysis beyond 10,000 h stability at 1.5 A cm^{-2}. Nature Communications, 16, 7236. doi:10.1038/s41467-025-62665-2.
- Yang, T. T., Patil, R. B., McKone, J. R., & Saidi, W. A. (2021). Revisiting trends in the exchange current for hydrogen evolution. Catalysis Science & Technology, 11(20), 6832–6838. doi:10.1039/D1CY01170G.
- Yang, X., Lin, L., Guo, X., & Zhang, S. (2024). Design of multifunctional electrocatalysts for ORR/OER/HER/HOR: Janus makes difference. Small, 20, 2404000. doi:10.1002/smll.202404000.
- Yi, H., Liu, S., Lai, C., Zeng, G., Li, M., Liu, X., Li, B., Huo, X., Qin, L., Li, L., Zhang, M., Fu, Y., An, Z., & Chen, L. (2021). Recent advance of transition-metal-based layered double hydroxide nanosheets: Synthesis, properties, modification, and electrocatalytic applications. Advanced Energy Materials, 11, 2002863. doi:10.1002/aenm.202002863.
- Zhai, P., Wang, C., Zhao, Y., Zhang, Y., Gao, J., Sun, L., & Hou, J. (2023). Regulating electronic states of nitride/hydroxide to accelerate kinetics for oxygen evolution at large current density. Nature Communications, 14, 1873. doi:10.1038/s41467-023-37091-x.
- Zhao, X., Zheng, X., Lu, Q., Li, Y., Xiao, F., Tang, B., Wang, S., Yu, D. Y. W., & Rogach, A. L. (2023). Electrocatalytic enhancement mechanism of cobalt single atoms anchored on different MXene substrates in oxygen and hydrogen evolution

reactions. EcoMat, 5(2), e12293. doi:10.1002/eom2.12293.

- Zhou, J., Shen, L., Costa, M. D., Persson, K. A., Ong, S. P., Huck, P., Lu, Y., Ma, X., Chen, Y., Tang, H., & Feng, Y. P. (2019). 2DMatPedia, an open computational database of two-dimensional materials from top-down and bottom-up approaches. Scientific Data, 6, 86. doi:10.1038/s41597-019-0097-3.
- Zhou, W., *et al.,*(2022). Regulating the scaling relationship for high catalytic kinetics and selectivity of the oxygen reduction reaction. Nature Communications, 13, 6414. doi:10.1038/s41467-022-34169-w.
- Zhou, W., Li, B., Liu, X., Jiang, J., Bo, S., Yang, C., An, Q., Zhang, Y., Soldatov, M. A., Wang, H., Wei, S., & Liu, Q. (2024). In situ tuning of platinum 5d valence states for four-electron oxygen reduction. Nature Communications, 15, 6650. doi:10.1038/s41467-024-51157-4.
- Zhu, D., Qiao, M., Liu, J., Tao, T., & Guo, C. (2020). Engineering pristine 2D metal–organic framework nanosheets for electrocatalysis. Journal of Materials Chemistry A, 8, 8143–8170. doi:10.1039/D0TA03138K.
- Zhu, J., Tu, Y., Cai, L., Ma, H., Chai, Y., Zhang, L., & Zhang, W. (2022). Defect-assisted anchoring of Pt single atoms on MoS_2 nanosheets produces high-performance catalyst for industrial hydrogen evolution reaction. Small, 18(4), 2104824. doi:10.1002/smll.202104824.
- Zhu, Q., Qu, Y., Liu, D., Ng, K. W., & Pan, H. (2020). Two-dimensional layered materials: High-efficient electrocatalysts for hydrogen evolution reaction. ACS Applied Nano Materials, 3(7), 6270–6296. doi:10.1021/acsanm.0c01331.
- Zou, X., & Zhang, Y. (2015). Noble metal-free hydrogen evolution catalysts for water splitting. Chemical Society Reviews, 44(15), 5148–5180. doi:10.1039/C4CS00448E.